

1
2
3
4
5
6
7
8
9
10
11
12
13
14
15
16
17
18
19
20
21
22
23
24
25

UNIVERSITY OF CALIFORNIA
SANTA CRUZ

**AN INCLUSIVE SEARCH FOR THE DECAY OF A BOOSTED
HIGGS BOSON IN THE $H \rightarrow b\bar{b}$ CHANNEL WITH THE ATLAS
DETECTOR**

A dissertation submitted in partial satisfaction of the
requirements for the degree of
DOCTOR OF PHILOSOPHY

in

PARTICLE PHYSICS

by

Jacob Martin Pasner

October 2019

The Dissertation of Jacob Martin Pasner
is approved:

Professor Jason Nielsen, Chair

Professor Abraham Seiden

Professor Michael Hance

Dean Lori Kletzer
Vice Provost and Dean of Graduate Studies

Copyright © by

Jacob Martin Pasner

2019

31 **Table of Contents**

32	List of Figures	vii
33	List of Tables	xi
34	Abstract	xii
35	Dedication	xiii
36	Acknowledgments	xiv
37	1 Introduction	1
38	I Theoretical Motivations and the Standard Model	2
39	2 The Standard Model and Beyond	3
40	2.1 The Standard Model	4
41	2.1.1 Bosons	5
42	2.1.2 Fermions	8
43	2.2 Quantum Electrodynamics	8
44	2.3 Quantum Chromodynamics	12
45	2.4 The Higgs Mechanism	14

46	2.4.1	Electroweak Symmetry Breaking	14
47	2.4.2	Fermion Mass Terms	18
48	2.4.3	The Higgs Boson	19
49	3	Boosted Higgs at the LHC	21
50	3.1	Higgs Production Mechanisms	22
51	3.2	Parton Distribution Function	25
52	3.3	Branching Ratios	26
53	3.4	Evidence for the SM Higgs	29
54	3.5	Boosted Higgs	32
55	II	Experimental Apparatus and Associated Facilities	34
56	4	The Large Hadron Collider	35
57	4.1	Particle Incjection Chain	36
58	4.2	LHC layout and design	38
59	4.3	Performance	41
60	4.4	Pile-up at the LHC	43
61	5	The ATLAS Detector	45
62	5.1	ATLAS Coordinate System	48
63	5.2	Tracking with the Inner Detector	52
64	5.2.1	Pixel Detector	54
65	5.2.2	Semiconductor Tracker	54
66	5.2.3	Transition Radiation Tracker	55
67	5.3	Calorimetry	56
68	5.3.1	Electromagnetic Calorimeter	57

69	5.3.2 Hadronic Calorimeter	59
70	5.4 Muon Spectrometer	61
71	III The HbbISR Analysis	64
72	6 Data and Simulation Preparation	65
73	6.1 Data Used	65
74	6.2 Monte Carlo Samples	65
75	7 Physics Object Selection	66
76	7.1 Calorimeter Jets	67
77	7.2 Track Jets	67
78	7.3 Fat Jets	67
79	7.4 B-tagged Jets	67
80	7.5 Muons	67
81	7.6 Overlap Removal	67
82	8 Event Selection	68
83	8.1 Selected Triggers	68
84	8.2 Pre-selection Studies	68
85	8.3 Signal Selection	68
86	8.4 Optimisation	68
87	9 Background Estimation	69
88	9.1 Multi-jet QCD estimation	69
89	9.2 $t\bar{t}$ control region	69
90	9.3 Single top estimation	69
91	9.4 Hadronic vector boson channel	69

92	10 Systematic Uncertainties	70
93	10.1 Theoretical Uncertainties	70
94	10.2 Experimental Uncertainties	70
95	11 Statistical Fit	71
96	11.1 Profile Likelihood Function	71
97	11.2 Fit Configuration	71
98	11.3 Statistical Tests	71
99	12 Results	72
100	12.1 Expectations	72
101	12.2 Statistical Analysis Results	72
102	12.3 Measurements and Limits	72
103	IV Conclusion	73
104	13 Conclusion	74
105	Bibliography	74
106	A Hadronic Vqq Sherpa Studies	78

107 List of Figures

108	2.1	Summary of several Standard Model total and fiducial production cross	
109		section measurements, corrected for leptonic branching fractions, com-	
110		pared to the corresponding theoretical expectations. All theoretical ex-	
111		pectations were calculated at NLO or higher. The dark-color error bar	
112		represents the statistical uncertainty. The lighter-color error bar repre-	
113		sents the full uncertainty, including systematics and luminosity uncer-	
114		tainties. The data/theory ratio, luminosity used and reference for each	
115		measurement are also shown. Uncertainties for the theoretical predictions	
116		are quoted from the original ATLAS papers. They were not always eval-	
117		uated using the same prescriptions for PDFs and scales. The Wgamma	
118		and Zgamma theoretical cross-sections have non-perturbative corrections	
119		applied to the NNLO fixed order calculations (PRD 87, 112003 (2013)).	
120		Not all measurements are statistically significant yet.	6
121	2.2	Table of all observed fundamental particles of the current Standard Model.	7
122	2.3	A lower dimensionality representation of the shape of the Higgs Potential.	
123		The central peak represents a $v = 0$ rotationally symmetric unstable	
124		state, while the trough represents the infinite choices of minima that can	
125		be selected upon the spontaneous breaking of symmetry.	15
126	3.1	Cross section for the production of the SM Higgs boson as a function of	
127		the center of mass energy (\sqrt{s}) at the LHC. [1]	22
128	3.2	Feynman diagrams representing the dominant Higgs production modes	
129		at the LHC.	23

130	3.3	[2] MMHT2014 NNLO PDFs at $Q^2 = 10\text{GeV}^2$ and $Q^2 = 10^4\text{GeV}^2$ with	
131		associated 68% confidence-level uncertainty bands. The colored regions	
132		indicate the probability of finding the labeled parton with a momentum	
133		fraction given along the x axis. As expected the u_V and d_V contain the	
134		largest fraction of the momentum, however we can also see that many	
135		gluons will exist with smaller fractions of the total momentum. Note	
136		that as Q^2 increases you are more likely to find something besides a u/d	26
137	3.4	Feynman diagrams representing the leading Higgs decay channels. . . .	28
138	3.5	Branching ratios for the decay of the SM Higgs boson near $m_H = 125\text{GeV}$	
139		including theoretical uncertainty bands [1]	29
140	3.6	Best fit values of $\sigma_i \cdot B^f$ for each specific channel $i \rightarrow H \rightarrow f$, as obtained	
141		from the generic parameterisation with 23 parameters for the combina-	
142		tion of the ATLAS and CMS measurements. The error bars indicate the	
143		1σ intervals. The fit results are normalised to the SM predictions for	
144		the various parameters and the shaded bands indicate the theoretical un-	
145		certainties in these predictions. Only 20 parameters are shown because	
146		some are either not measured with a meaningful precision, in the case of	
147		the $H \rightarrow ZZ$ decay channel for the WH , ZH , and $t\bar{t}H$ production pro-	
148		cesses, or not measured at all and therefore fixed to their corresponding	
149		SM predictions, in the case of the $H \rightarrow b\bar{b}$ decay mode for the ggF and	
150		VBF production processes [3].	30
151	3.7	Best fit results for the production signal strengths for the combination of	
152		ATLAS and CMS data. Also shown are the results from each experiment.	
153		The error bars indicate the 1σ (thick lines) and 2σ (thin lines) intervals.	
154		The measurements of the global signal strength μ are also shown [3]. . .	31
155	3.8	Best fit results for the decay signal strengths for the combination of AT-	
156		LAS and CMS data. Also shown are the results from each experiment.	
157		The error bars indicate the 1σ (thick lines) and 2σ (thin lines) intervals [3].	32
158	4.1	CERN accelerator complex	37
159	4.2	Labeled diagram of all the experiments at the LHC indicating the counter	
160		circulating beams and points of interest along the circumference of the	
161		accelerator.	39
162	4.3	Depiction of a LHC dipole magnet 2-in-1 design labeling the major com-	
163		ponents	40

164	4.4	Luminosity is monitored as both a running total known as the Integrated	
165		Luminosity as depicted in (a) and as an instantaneous quantity as shown	
166		in (b)	43
167	4.5	Pileup for data taking periods 2015 - 2018	44
168	5.1	[6] Here we see a cut-away side view of the ATLAS detector with the	
169		major components labeled. Note that within each of these labeled com-	
170		ponents there may exist multiple different detector technologies. For scale	
171		two people in red are shown standing between the disk muon chambers	
172		on the left side of the figure.	46
173	5.2	This slice of the ATLAS detector depicts how different particles interact	
174		with each component of the detector it crosses. A dashed line indicates	
175		no interaction while a solid line indicates interaction. Electrons (yel-	
176		low/green) and charged hadrons (red) interact with the tracker and curve	
177		in the solenoid's magnetic field. Electrons and photons (yellow/green) are	
178		absorbed by the Electromagnetic calorimeter. All hadrons (red/yellow)	
179		are absorbed by the Hadronic calorimeter. The muons (orange) curve in	
180		both the solenoid and torroid magnetic fields before exiting the detector.	
181		Finally, the neutrinos (white) pass through the entire detector without	
182		interacting.	49
183	5.3	[7] A cartoon view of the the LHC from above showing the SPS, LHC	
184		and the four main experiments of the LHC: ATLAS, CMS, LHCb, and	
185		ALICE. The standard cartesian coordinate system is shown with its origin	
186		at the ATLAS interaction point, the positive x -axis towards the center	
187		of the LHC, the positive y -axis pointing upwards, and the positive z -axis	
188		pointing along the beamline towards the "A-side"	50
189	5.4	Modified from [7] this cartoon represents a selection of pseudorapidity	
190		(η) values overlaid with some cartesian coordinates (dashed black lines).	
191		The redlines are drawn for $\eta = \pm 0.5, 1.0, 3.0$	51
192	5.5	[8] Diagram of inner detector	52
193	5.6	[11] Schematic of the Inner Detector including eta lines. Each component	
194		shown is cylindrically symmetric leading to a multi-layered detector. . .	53
195	5.7	[6] A cutaway diagram of ATLAS's sampling calorimeters	56
196	5.8	[6] Sketch of LAr EMC barrel module where the lead and liquid argon	
197		layers are visible in an accordion like geometry. Looking from the fore-	
198		ground to the back there are 3 different types of cells visible.	58

199	5.9	[6] Schematic of a tile calorimeter module including a depiction of the con-	
200		nection between the scintillator tile to the photomultiplier via a wavelength-	
201		shifting fibre.	60
202	5.10	[6] A cut-away diagram of the ATLAS muon system and its many sub-	
203		detectors.	62

204 List of Tables

205	3.1	SM Higgs boson production cross sections in units of pb for $m_H =$	
206		125 GeV in pp collisions as a function of the center-of-mass energy, \sqrt{s} ,	
207		at the LHC. The predictions for the ggF channel include the latest N3LO	
208		results leading to reduced theoretical uncertainties by a factor around 2	
209		compared to the N2LO results [1].	24
210	3.2	The branching ratios and the relative uncertainty for a Standard Model	
211		Higgs boson with $m_H = 125$ GeV [1].	27

212

Abstract

213

An Inclusive Search for the decay of a Boosted Higgs boson in the $H \rightarrow b\bar{b}$

214

channel with the ATLAS detector

215

by

216

Jacob Martin Pasner

217

Abstract placeholder

218

Dedication

219

Dedication

220

Dedication

Acknowledgments

222 **Chapter 1**

223 **Introduction**

224 Every dissertation should have an introduction. You might not realize it, but the
225 introduction should introduce the concepts, backgrouand, and goals of the dissertation.

226

Part I

227

Theoretical Motivations and the

228

Standard Model

Chapter 2

The Standard Model and Beyond

The Standard Model (SM) of Particle Physics is humanities best "guess" at the force laws that describe the observed behavior of all particles in our universe. Its formulation is a collection of Quantum Field Theories (QFT) that describe the following interactions of elementary matter in Nature: the electromagnetic force, the weak nuclear force and the strong nuclear force. Gravity is noticeably absent as currently there is no viable quantum theory for observed gravitational effects. The Glashow-Salam-Weinberg (GSW) theory of Quantum Electrodynamics (QED) describes the electromagnetic and weak forces, while Quantum Chromodynamics (QCD) describes the strong force. These theories form the following symmetry group of the Standard Model.

$$\underbrace{\mathrm{SU}_C(3)}_{\mathrm{QCD}} \otimes \underbrace{\mathrm{SU}_L(2) \otimes \mathrm{U}_Y(1)}_{\mathrm{GSW}}. \quad (2.1)$$

240 The gauge principle states that the SM Lagrangian and its predictions must be invariant
241 under local transformations using an operator from any of these constituent groups.
242 Thus, any theory must only include transformations and terms that maintain the local
243 invariance of the complete Lagrangian. In particular, this requirement was violated
244 by any attempt to include an explicit mass term for the Gauge Bosons of QED and
245 for all fermions. Around 1960 a possible solution to this lack of mass was proposed
246 in the form of the spontaneous breaking of the ElectroWeak symmetry, now known as
247 the Higgs mechanism. In the following sections I will go into more detail about the
248 Lagrangian formalism of the Standard Model, QCD, QED and this recently verified
249 Higgs Mechanism.

250 **2.1 The Standard Model**

251 At the turn of the 20th century our understanding of the constituent matter of the uni-
252 verse was limited to what we could see with microscopes and imply from the observations
253 of light and electricity, giving us evidence for both the photon and the electron. In the
254 first half of the century we discovered the field of subatomic physics with Rutherford's
255 1911 gold foil scattering experiment, and Dirac successfully demonstrated the quantiza-
256 tion of the electromagnetic field, the first step towards a fully Gauge Invariant Quantum
257 Field Theory. In the second half we literally delved deeper, discovering that the nucleus
258 contained structure and extended our theories to include the the complex mechanics of
259 quarks and gluons. With the discovery of the Higgs in 2013 the Standard Model has

260 become an irrefutable framework as can be seen in the high level of agreement between
261 theory and experiment in fig. 2.1.

262 The QCD and QED theories predict two classes of particles: fermions and bosons shown
263 in fig. 2.2. These particles represent the quanta of the quantum fields of the Standard
264 Model and the mediators of the fundamental forces of Nature.

265 **2.1.1 Bosons**

266 These spin-1 particles are known as the vector gauge bosons and are the force carriers
267 of the SM. The most commonly known is the electromagnetic force's un-charged and
268 massless photon (γ) which interacts with all charged particles and is often referred to
269 as "light". The weak nuclear force is involved in nuclear interactions such as beta
270 decays and is carried by 3 bosons all of which have mass and couple to all fermions;
271 the W^\pm bosons, which mediate the charged weak nuclear interaction and allow for
272 flavor changing currents; and the Z boson which mediates the neutral weak nuclear
273 interaction. Finally we have 8 massless gluons which mediate the strong nuclear force
274 and only interact with fermions with a "color" charge such as the quarks contained
275 inside the nucleus. The only spin-0 boson, the Higgs Boson (h) is the key to generating
276 mass terms in the SM Lagrangian for the massive Gauge Bosons and for fermions.
277 This is done through the so called Higgs Mechanism and is discussed in more detail in
278 section 2.4.

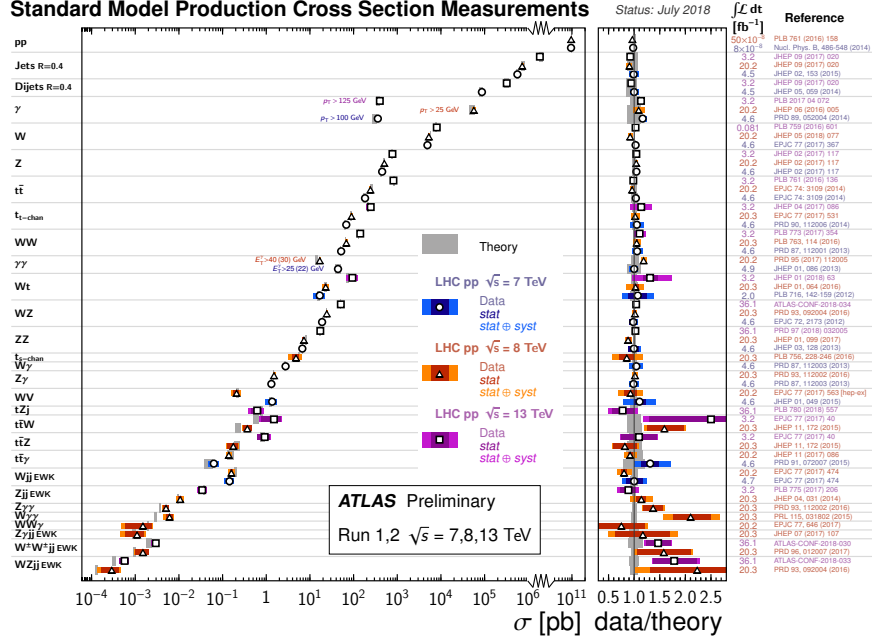


Figure 2.1: Summary of several Standard Model total and fiducial production cross section measurements, corrected for leptonic branching fractions, compared to the corresponding theoretical expectations. All theoretical expectations were calculated at NLO or higher. The dark-color error bar represents the statistical uncertainty. The lighter-color error bar represents the full uncertainty, including systematics and luminosity uncertainties. The data/theory ratio, luminosity used and reference for each measurement are also shown. Uncertainties for the theoretical predictions are quoted from the original ATLAS papers. They were not always evaluated using the same prescriptions for PDFs and scales. The $W\gamma$ and $Z\gamma$ theoretical cross-sections have non-perturbative corrections applied to the NNLO fixed order calculations (PRD 87, 112003 (2013)). Not all measurements are statistically significant yet.

Standard Model of Elementary Particles

three generations of matter (fermions)						interactions / force carriers (bosons)			
LEPTONS	I		II		III				
	mass	charge	spin	mass	charge	spin	mass	charge	
	spin	charge	spin	spin	charge	spin	spin	charge	
	spin	charge	spin	spin	charge	spin	spin	charge	
QUARKS	$\approx 2.2 \text{ MeV}/c^2$	$\frac{2}{3}$	$\frac{1}{2}$	$\approx 1.28 \text{ GeV}/c^2$	$\frac{2}{3}$	$\frac{1}{2}$	$\approx 173.1 \text{ GeV}/c^2$	0 0 1	
	u	up	c	charm	t	top	g	gluon	
	$\approx 4.7 \text{ MeV}/c^2$	$-\frac{1}{3}$	$\frac{1}{2}$	$\approx 96 \text{ MeV}/c^2$	$-\frac{1}{3}$	$\frac{1}{2}$	$\approx 4.18 \text{ GeV}/c^2$	0 0 1	
LEPTONS	$\approx 0.511 \text{ MeV}/c^2$	-1	$\frac{1}{2}$	$\approx 105.66 \text{ MeV}/c^2$	-1	$\frac{1}{2}$	$\approx 1.7768 \text{ GeV}/c^2$	0 0 1	
	e	electron	μ	muon	τ	tau	Z	Z boson	
	$< 2.2 \text{ eV}/c^2$	0	$\frac{1}{2}$	$< 0.17 \text{ MeV}/c^2$	0	$\frac{1}{2}$	$< 18.2 \text{ MeV}/c^2$	± 1 1	
	ν_e	electron neutrino	ν_μ	muon neutrino	ν_τ	tau neutrino	W	W boson	
						GAUGE BOSONS VECTOR BOSONS			

Figure 2.2: Table of all observed fundamental particles of the current Standard Model.

279 2.1.2 Fermions

280 These spin-1/2 particles can be further broken up into two distinct families of particles,
281 the leptons and the quarks, both of which contain three "generations" each with an "up"
282 and "down" type particle. The leptons "up" type members are the electrically charged
283 electron (e), muon (μ) and tau (τ) while the "down" type are their electrically neutral
284 counterparts ν_e , ν_μ , ν_τ . The quarks "up" type members are the up (u), charm (c),
285 and top (t) each with a $+2/3$ elementary charge, while the "down" type members are
286 the down (d), strange (s), and bottom (b) all of which have a $-1/3$ elementary charge.
287 Each quark carries a "color" charge thus allowing them to participate in strong force
288 interactions. Due to the observed color confinement of the strong force these quarks are
289 only observed in colorless bound states known as "mesons" (1 quark and 1 anti-quark)
290 and "baryons" (an odd number of quarks and anti-quarks). All of the above fermions
291 have an anti-particle partner which has the opposite electrical charge but is otherwise
292 identical.

293 2.2 Quantum Electrodynamics

294 In the SM the Electromagnetic and Weak nuclear forces are unified into the Electroweak
295 interaction which is represented by the $SU(2)_L \times U(1)_Y$ gauge group. The L represents
296 the physical observable that the Weak interaction, and thus the $SU(2)$ transformation,
297 only acts on left handed particle states. The Y states that this is the $U(1)$ symmetry

298 for the weak hypercharge Y instead of the electromagnetic charge. The particle states
 299 for these interactions are solutions to the Dirac equation and are represented as Dirac
 300 spinor doublets (Ψ_L) for the left handed states, and as Dirac spinor singlets (Ψ_R) for
 301 the right handed states. Thus when a general transformation from the Electroweak
 302 gauge group is applied to the left handed spinor doublet you get eq. (2.2)

$$\Psi_L \rightarrow \Psi'_L = \exp \left(\underbrace{ig' \frac{Y_L}{2} \zeta(x)}_{U(1)_Y} + \underbrace{ig_W \boldsymbol{\alpha}(x) \cdot \mathbf{T}}_{SU(2)_L} \right) \Psi_L. \quad (2.2)$$

303 For the right handed spinor singlet the $SU(2)_L$ doesn't contribute and you get eq. (2.3)

$$\Psi_R \rightarrow \Psi'_R = \exp \left(\underbrace{ig' \frac{Y_R}{2} \zeta(x)}_{U(1)_Y} \right) \Psi_R. \quad (2.3)$$

304 We can see that these local gauge transformations have introduced space-time depen-
 305 dant terms $\boldsymbol{\alpha}(x)$ and $\zeta(x)$ into our electroweak Lagrangian. Due to the derivatives
 306 contained within the kinetic term of this lagrangian, this new configuration would in-
 307 troduce additional terms, thus violating our required local gauge invariance. Luckily,
 308 we can remove these additional terms by replacing the standard derivative (∂_μ) with th
 309 covariant derivative (D_μ) as seen in eq. (2.4) for the left handed states and eq. (2.5) for
 310 the right handed states.

$$D_\mu = \partial_\mu - \underbrace{\frac{1}{2}ig' B_\mu Y_L}_{U(1)_Y} - \underbrace{\frac{1}{2}ig_W \mathbf{W}_\mu \cdot \boldsymbol{\tau}}_{SU(2)_L} \quad (2.4)$$

$$D_\mu = \partial_\mu - \underbrace{\frac{1}{2}ig' B_\mu Y_R}_{U(1)_Y} \quad (2.5)$$

311 Here we see two new gauge fields; B_μ the weak hypercharge field and \mathbf{W}_μ the charged
 312 weak field as well as the associated coupling constants g', g_W, Y_L, Y_R and the $SU(2)$
 313 generators $\boldsymbol{\tau}$. Next we write down the transformation properties of these new fields

$$\mathbf{W}_\mu(x) \rightarrow \mathbf{W}'_\mu(x) = \mathbf{W}_\mu + \partial_\mu \boldsymbol{\alpha}(x) + g_W \mathbf{W}_\mu(x) \times \boldsymbol{\alpha}(x) \quad (2.6)$$

$$B_\mu \rightarrow B'_\mu = B_\mu + \frac{1}{g'} \partial_\mu \zeta(x) \quad (2.7)$$

314 The form of these fields is chosen such that the final Lagrangian is invariant under
 315 $SU(2)_L \times U(1)_Y$ transformations, and thus we have restored gauge invariance for the
 316 kinetic term of our electroweak Lagrangian! Inserting these new definitions into the
 317 Lagrangian for the spinor field Ψ which satisfies the free-particle Dirac equation we get

$$\mathcal{L} = i\bar{\Psi}_L \gamma^\mu \left(\partial_\mu - \frac{1}{2}ig' B_\mu Y_L - \frac{1}{2}ig_W \mathbf{W}_\mu \cdot \boldsymbol{\tau} \right) \Psi_L + i\bar{\Phi}_R \gamma^\mu \left(\partial_\mu - \frac{1}{2}ig' B_\mu Y_R \right) \Phi_R \quad (2.8)$$

318 Next we must construct the gauge field self interaction and mass terms

$$\mathcal{L} = -\frac{1}{4}\mathbf{F}_{\mu\nu}\mathbf{F}^{\mu\nu} - \frac{1}{4}B_{\mu\nu}B^{\mu\nu} + \frac{1}{2}M_W^2\mathbf{W}_\mu\mathbf{W}^\mu + \frac{1}{2}M_B^2B_\mu B^\mu \quad (2.9)$$

319 where the field tensors $\mathbf{F}^{\mu\nu}$ and $B^{\mu\nu}$ are defined to be

$$\mathbf{F}^{\mu\nu} = \partial^\mu\mathbf{W}^\nu - \partial^\nu\mathbf{W}^\mu + g\mathbf{W}^\mu \times \mathbf{W}^\nu \quad (2.10)$$

$$B^{\mu\nu} = \partial^\mu B^\nu - \partial^\nu B^\mu \quad (2.11)$$

320 The field tensor terms in eq. (2.9) are invariant under our gauge transformations, but
 321 simply plugging in eq. (2.4) or eq. (2.5) into the mass terms shows that these terms
 322 violate gauge invariance thus implying $M_W = 0$ and $M_B = 0$ in direct contradiction of
 323 the observed masses of the weak gauge bosons. This issue arises again for fermion mass
 324 terms as illustrated below for the electron field (e) expanded in its chiral basis.

$$m_e\bar{e}e = m_e \begin{pmatrix} e_R^\dagger & e_L^\dagger \end{pmatrix} \begin{pmatrix} e_L \\ e_R \end{pmatrix} = m_e(e_R^\dagger e_L + e_L^\dagger e_R) \quad (2.12)$$

325 Remembering that the left and right handed spinors of the electroweak interaction trans-
 326 form differently we see that this mixture of right and left fields violates gauge invariance.
 327 This again forces us to conclude that $m_e = 0$ in contradiction to the observation that
 328 the electron does indeed have mass. As mentioned in section 2.1.1 the resolution to
 329 these mass mysteries lies in the Higgs mechanism discussed in section 2.4

330 2.3 Quantum Chromodynamics

331 Quantum Chromodynamics is the continuation of the mathematical framework estab-
 332 lished by Quantum Electrodynamics (section 2.2, this time for the strong force described
 333 by the $SU(3)_C$ gauge group where the C represents the "color" charge of QCD. This
 334 color charge doesn't imply actual visible color, but is useful as an analogy to the visible
 335 spectrum where a combination of red, green, and blue generates white. For QCD the
 336 combination of red, green, and blue color charges results in a colorless object. As men-
 337 tioned in section 2.1.2 the quarks will contain a color (anti-color) charge represented by
 338 a color triplet field which transforms under the general $SU(3)$ transformation as shown
 339 here

$$q = \begin{pmatrix} q_r \\ q_g \\ q_b \end{pmatrix} \rightarrow q' = \exp \left(ig_s \sum_{k=1}^8 \eta_k(x) \frac{\lambda_k}{2} \right) q \quad (2.13)$$

340 Here the λ_k are the generators for $SU(3)$, $\eta(x)_k$ is the space-time dependency for each
 341 generator, and g_s is the strong coupling constant. As with QED, the introduction of
 342 these space-time dependant terms introduces new terms into the kinematic portion of
 343 the lagrangian thus spoiling our gauge invariance. Again, we introduce a covariant

344 derivative to restore invariance

$$D_\mu = \partial_\mu - ig_s G_\mu^k \frac{\lambda_k}{2} \quad (2.14)$$

345 Here the G_μ^k are the new fields introduced for the 8 gluons. These new fields transform
346 under $SU(3)$ as shown in eq. (2.15)

$$G_\mu^k \rightarrow G_\mu'^k = G_\mu^k + \partial_\mu \eta_k(x) + g_s f_{klm} \eta_l(x) G_\mu^m \quad (2.15)$$

347 Given these definitions we can construct the QCD Lagrangian (\mathcal{L}_{QCD}) as shown in
348 eq. (2.16) where the gluon field tensor $G_k^{\mu\nu}$ is the one defined in eq. (2.17)

$$\mathcal{L}_{QCD} = \bar{q}(i\gamma_\mu D^\mu - m_q)q - \frac{1}{4} G_k^{\mu\nu} G_{k\mu\nu} \quad (2.16)$$

$$G_k^{\mu\nu} = \partial^\mu G_k^\nu - \partial^\nu G_k^\mu + g_s f_{klm} G^\mu G_m^\nu \quad (2.17)$$

349 The strong force is peculiar in that we experimentally observe only colorless objects in
350 the form of bound states of quarks known as hadrons. Qualitatively, when a bound
351 state of quarks (meson or baryon) is given suffieint energy to separate the strong force
352 dramatically increases in strength. At the point where the objects would separate, and
353 thus no longer be colorless, it becomes energetically favorable to produce a quark/anti-
354 quark pair in a process known as hadronization. In other words, attempting to separate

355 a bound quark state into its colored constituents simply results in new colorless bound
 356 states. This requirement of colorless objects by the strong force is known as color
 357 confinement. For highly energetic strong interactions at hadron colliders the result is
 358 an expanding chain of hadronizing quarks and gluons and their decay products known
 359 as a jet.

360 **2.4 The Higgs Mechanism**

361 The Higgs Mechanism is the system by which the gauge bosons and fermions attain mass
 362 through the spontaneous breaking of the electroweak symmetry of the Higgs potential.
 363 This section will also discuss briefly the couplings of the Higgs boson to massive particles,
 364 as well as it's self couplings.

365 **2.4.1 Electroweak Symmetry Breaking**

366 The Higgs field is expressed as a complex doublet, Φ , and thus has four components as
 367 shown in eq. (2.18)

$$\Phi(x) = \begin{pmatrix} \phi^+ \\ \phi^0 \end{pmatrix} = \frac{1}{\sqrt{2}} \begin{pmatrix} \phi_1(x) + i\phi_2(x) \\ \phi_3(x) + i\phi_4(x) \end{pmatrix} \quad (2.18)$$

368 The four compoenents of this field each represent a degree of freedom which will be
 369 used to give the longitudinal polarizations of the gauge bosons W^\pm, Z and the mass of

the Higgs boson. The resulting lagrangian for the higgs includes a kinetic term (K) as well as the Higgs potential (V) all of which are invariant under the Electroweak gauge symmetry $SU(2)_L \times U(1)_Y$

$$\mathcal{L}_{\text{Higgs}} = \underbrace{(D_\mu \Phi)^\dagger D^\mu \Phi}_{\text{K}} - \underbrace{(\mu^2 \Phi^\dagger \Phi + \lambda (\Phi^\dagger \Phi)^2)}_{\text{V}} \quad (2.19)$$

Here we constrain $\mu^2 < 0$ and $\lambda > 0$ such that the potential forms a stable minima. The shape of this potential is shown in fig. 2.3 and is often referred to as the "Mexican-hat" or "Wine-bottle" potential.

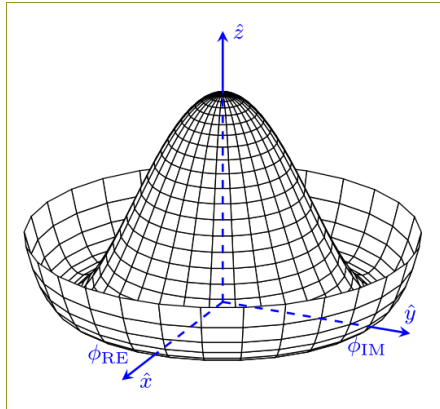


Figure 2.3: A lower dimensionality representation of the shape of the Higgs Potential. The central peak represents a $v = 0$ rotationally symmetric unstable state, while the trough represents the infinite choices of minima that can be selected upon the spontaneous breaking of symmetry.

Whatever you call it, this potential is significant in that its minimum is not at $\Phi = 0$ but instead is symmetric around the origin thus defining an infinite number of states

378 that minimize V . The value of this minima can be calculated by taking the derivative
 379 of V with respect to Φ and setting it equal to 0. This value, also known as the vacuum
 380 expectation value (vev) has been found to be $v \equiv \sqrt{-\mu^2/\lambda} = 246$ GeV. In order to reach
 381 this ground state energy, the Higgs field must spontaneously break this symmetry, and
 382 thus acquire an arbitrary single value. For ease of calculation we orient our coordinate
 383 system such that

$$\langle \Phi(x) \rangle = \frac{1}{\sqrt{2}} \begin{pmatrix} 0 \\ v \end{pmatrix} \quad (2.20)$$

384 Next we parameterize small perturbations around the minimum of the Higgs potential
 385 as

$$\langle \Phi(x) \rangle = \frac{1}{\sqrt{2}} \begin{pmatrix} 0 \\ v + h(x) \end{pmatrix} \exp \left(i \frac{\tau^i}{2} \theta^i(x) \right) \quad (2.21)$$

386 Here the real scalar field $h(x)$ corresponds to radial perturbations of the minima and
 387 while the three $\theta^i(x)$ are the Nambu-Goldstone fields with values determined by your
 388 choice of gauge. Choosing the unitary gauge of $\theta^i(x) = 0$ and expanding the kinetic

389 term of eq. (2.19) around the vev we get

$$\mathcal{L}_{\text{Higgs},K} = \frac{g^2 v^2}{8} \left((W_\mu^-)^\dagger W^{-\mu} + (W_\mu^+)^\dagger W^{+\mu} \right) + \frac{1}{2} \begin{pmatrix} W_\mu^{3\dagger} & B_\mu^\dagger \end{pmatrix} \mathbf{M}^2 \begin{pmatrix} W^{3\mu} \\ B^\mu \end{pmatrix} + \dots \quad (2.22)$$

390 Here the first term is the physical mass term for the W^\pm bosons where we have con-
 391 structed their charge eigenstates out of the $W^{1,2}$ fields like this $W^\pm = \frac{1}{\sqrt{2}}(W^1 \mp iW^2)$.
 392 The second term represents the mixture of the W^3 and B fields through the mass ma-
 393 trix \mathbf{M} . By diagonalizing this matrix and identifying the mass eigenstates we find the
 394 physical fields of the photon (γ) and the Z boson

$$\mathbf{M}_{\text{Diagonalized}}^2 = \begin{pmatrix} 0 & 0 \\ 0 & \frac{v^2}{4}(g_W^2 + g'^2) \end{pmatrix} \quad (2.23)$$

395 The upper left diagonal element corresponds to the massless photon while the lower
 396 right diagonal element gives the mass of the massive Z boson. This leaves us with the
 397 following masses for the 4 Electroweak bosons

$$m_W = \frac{1}{2} g_W v \quad , \quad m_Z = \frac{1}{2} v \sqrt{g_W^2 + g'^2} \quad , \quad m_\gamma = 0 \quad (2.24)$$

398 The masses of the W^\pm and Z gauge bosons can be related through the Weinberg angle

399 or mixing angle which

$$\theta_W = \cos^{-1} \left(\frac{g_W}{\sqrt{g_W^2 + g'^2}} \right) \rightarrow m_Z = \frac{m_W}{\cos \theta_W} \quad (2.25)$$

400 Using this definition we can write out the exact mixture of B and W^3 that make up the
401 photon and Z boson

$$\gamma = \cos(\theta_W)B + \sin(\theta_W)W^3 \quad (2.26)$$

$$Z = -\sin(\theta_W)B + \cos(\theta_W)W^3 \quad (2.27)$$

402 2.4.2 Fermion Mass Terms

403 In section 2.2 we saw that fermion mass terms violate gauge invariance due to the
404 mixing of the left and right chiral states. The Higgs mechanism again allows for a gauge
405 invariant method of generating mass terms but this time through the Yukawa coupling
406 of the Higgs field to the fermion fields. To see an example of this here is the Yukawa
407 coupling term for the electron doublet (Ψ_L) and singlet (Ψ_R) coupling to the Higgs field
408 (Φ) after spontaneous symmetry breaking giving it the form shown in eq. (2.21) where
409 we have again choosen the unitary gauge $\Phi^i(x) = 0$.

$$\mathcal{L}_{Yukawa} = -g_e \left[\bar{\Psi}_L \Phi \Psi_R + \bar{\Psi}_R \Phi^\dagger \Psi_L \right] \quad (2.28)$$

$$= -\frac{g_e}{\sqrt{2}} \left[\begin{pmatrix} \bar{\nu}_e & \bar{e} \end{pmatrix}_L \begin{pmatrix} 0 \\ \nu + h \end{pmatrix} e_R + \bar{e}_R \begin{pmatrix} 0 & (\nu + h) \end{pmatrix} \begin{pmatrix} \nu_e \\ e \end{pmatrix}_L \right] \quad (2.29)$$

$$= -\underbrace{\frac{g_e}{\sqrt{2}} \nu}_{m_e} (\bar{e}_L e_R + \bar{e}_R e_L) - \underbrace{\frac{g_e}{\sqrt{2}} h}_{g_{e,h}} (\bar{e}_L e_R + \bar{e}_R e_L) \quad (2.30)$$

410 And voila, we have successfully generated mass terms for our fermion field and main-
 411 tained the gauge invariance of our Lagrangian by using all gauge invariant fields. This
 412 operation has also left us with the second term which represents the coupling of the
 413 electron to the higgs itself thus giving us the form of it's coupling constant $g_{e,h}$. Using
 414 our newly found mass of the electron m_e we can write

$$g_{e,h} = \frac{g_e}{\sqrt{2}} = \frac{m_e}{\nu} \quad (2.31)$$

415 Thus we see that the coupling of the higgs boson to a fermion is indeed proportional to
 416 the mass of the fermion itself. In other words, the more massive a particle is, the more
 417 the higgs couples to it and vice versa.

418 2.4.3 The Higgs Boson

419 As we have seen this Higgs mechanism not only properly mixes the gauge fields thus
 420 providing them gauge invariant mass terms, it also properly combines the left and right

421 chiral states of fermions to produce their mass terms. The final step then is to determine
 422 an observable of the theory that can be tested in experiment, namely the existence of a
 423 massive scalar particle, the Higgs boson itself.

424 Turning our attention to the potential term (V) of eq. (2.19) and substituting in our
 425 definition for Φ given in eq. (2.21) we find

$$\mathcal{L}_{\text{Higgs,V}} = \frac{1}{2}\mu^2\nu^2 - \mu^2h^2 + \lambda\nu h^3 + \frac{1}{4}\lambda h^4 \quad (2.32)$$

426 Here the first term is constant and thus can be ignored. The second term is the mass
 427 term for the SM particle the Higgs boson, $m_h = \sqrt{-2\mu^2} = \sqrt{2\lambda}\nu$. Remembering that
 428 $h = h(x)$ was used for small radial perturbations of the Higgs field we can identify the
 429 Higgs boson simply as an excitation of the Higgs field. Finally, the third and fourth
 430 terms represent the Higgs boson self-couplings. With these couplings and mass terms
 431 in hand we can now move on to the experimental verification of this theory as discussed
 432 next in chapter 3.

433 Chapter 3

434 Boosted Higgs at the LHC

435 In chapter 2 I've shown how the higgs mechanism resolves inconsistencies of the model
436 surrounding the generation of gauge boson and fermion mass terms while also main-
437 taining gauge invariance. However to understand the search for and resulting discovery
438 of this SM Higgs boson requires the discussion of how one goes about producing and
439 detecting the physical object itself. In order to gather sufficient statistics to validate
440 the theory we require a collider capable of putting enough energy into a collision to
441 rapidly produce Higgs bosons for study. To this end the Large Hadron Collider (LHC)
442 discussed in chapter 4 was laboriously designed, funded, and constructed by the largest
443 international collaboration of scientists on the planet. In this chapter I will discuss the
444 relevant Higgs boson production mechanisms available at the LHC as well as the various
445 decay modes of the Higgs that were used for its discovery, and are currently used to
446 measure its properties.

3.1 Higgs Production Mechanisms

At the LHC the dominate production mechanisms for the higgs in order of decreasing cross section are: gluon-fluon fusion (ggF), vector boson fusion (VBF), vector boson associated production or “Higgsstrahlung” (VH), and associated production with $t\bar{t}$ ($t\bar{t}H$) and $b\bar{b}$ ($b\bar{b}H$). The cross sections with associated theoretical uncertainties for each is shown as a function of the center of mass energy \sqrt{s} in fig. 3.1 and the actual feynman diagrams can be seen in fig. 3.2. For reference the exact produciton cross sections for a variety of center of mass energies are detailed in table 3.1.

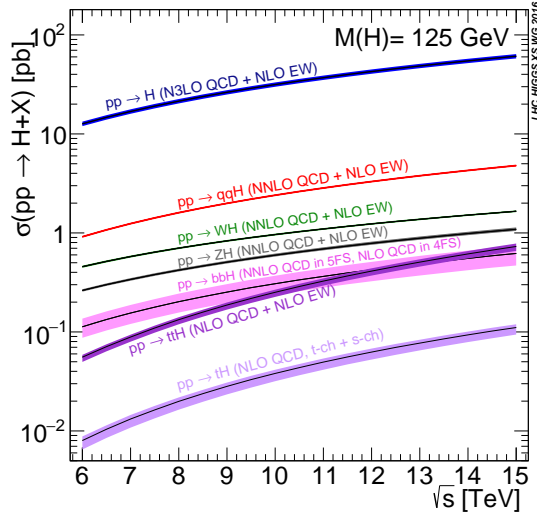


Figure 3.1: Cross section for the production of the SM Higgs boson as a function of the center of mass energy (\sqrt{s}) at the LHC. [1]

The dominant Higgs production mechanism at hadron colliders is ggF. This may seem strange as gluons are massless and thus do not couple directly to the Higgs. Instead the

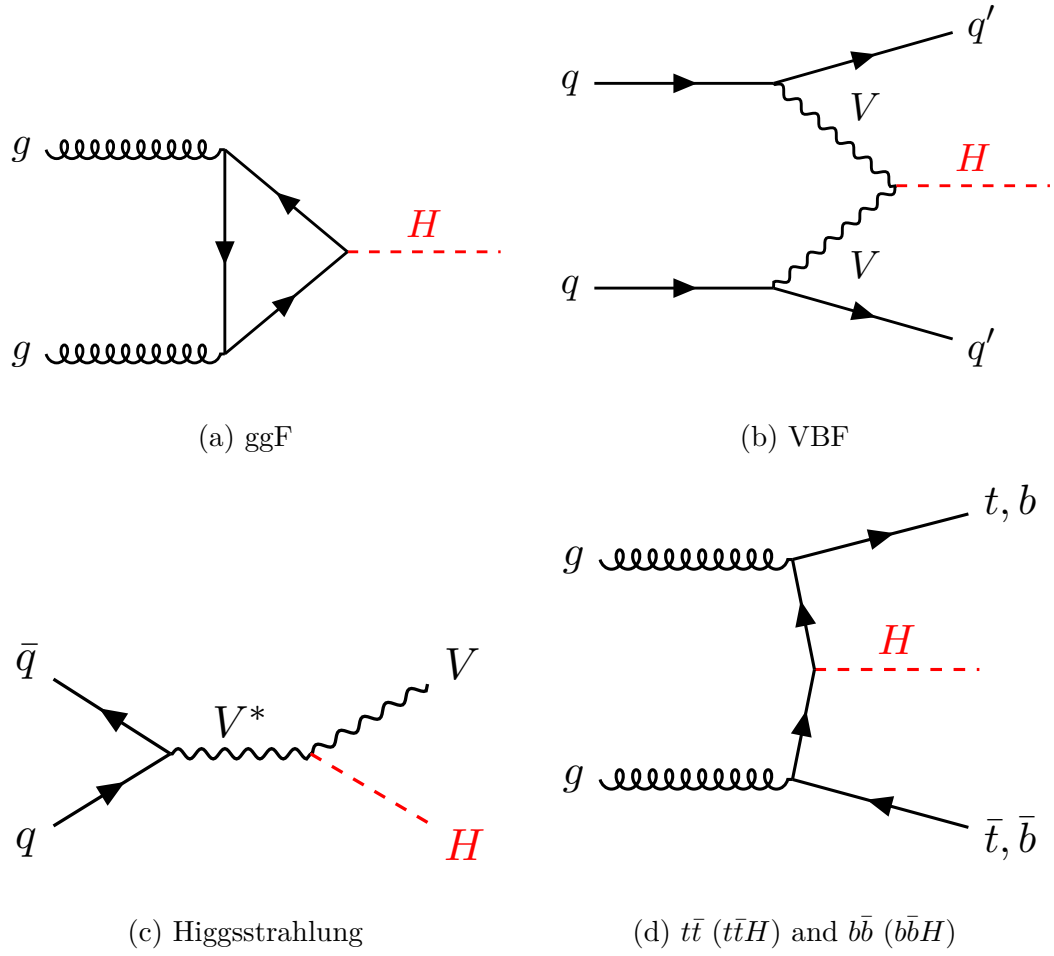


Figure 3.2: Feynman diagrams representing the dominant Higgs production modes at the LHC.

Table 3.1: SM Higgs boson production cross sections in units of pb for $m_H = 125$ GeV in pp collisions as a function of the center-of-mass energy, \sqrt{s} , at the LHC. The predictions for the ggF channel include the latest N3LO results leading to reduced theoretical uncertainties by a factor around 2 compared to the N2LO results [1].

\sqrt{s} (TeV)	ggF	VBF	WH	ZH	$t\bar{t}H$	Total (pb)
8	$21.4^{+5\%}_{-5\%}$	$1.60^{+2\%}_{-2\%}$	$0.70^{+3\%}_{-3\%}$	$0.42^{+5\%}_{-5\%}$	$0.13^{+8\%}_{-13\%}$	24.2
13	$48.6^{+5\%}_{-5\%}$	$3.78^{+2\%}_{-2\%}$	$1.37^{+2\%}_{-2\%}$	$0.88^{+5\%}_{-5\%}$	$0.50^{+9\%}_{-13\%}$	55.1
14	$54.7^{+5\%}_{-5\%}$	$4.28^{+2\%}_{-2\%}$	$1.51^{+2\%}_{-2\%}$	$0.99^{+5\%}_{-5\%}$	$0.60^{+9\%}_{-13\%}$	62.1

457 gluons indirectly couple to the Higgs via a quark loop. As discussed in section 2.4.2, the
458 coupling of a fermion is proportional to m_f so the dominant contribution to this quark
459 loop comes from the top quark.

460 The second largest cross section for Higgs production at the LHC comes from the VBF
461 mechanism. In VBF the initial state quarks scatter via the exchange of a W^\pm or
462 Z boson which subsequently radiates the Higgs boson. Unlike ggF this production
463 mechanism scatters the initial state quarks which allows them to be observed as part of
464 the interaction. The existence of these extra quarks makes these interactions easier to
465 select for during analysis.

466 Next we have Higgs production in association with a vector boson. The cross section for
467 this is even lower than the above two, but remains important due to the easily selected
468 signature of the decaying vector boson. The largest background at the LHC is multijet
469 events coming from interactions that produce strong force objects. Thus the leptons

470 from the boson's decay act as a discriminator from this multijet background greatly
471 reducing its effect on sensitivity.

472 With the lowest cross section of the four methods discussed we have the production of
473 the Higgs in association with either $b\bar{b}$ or $t\bar{t}$. This channel is important due to our
474 ability to measure not only the Higgs, but also the quarks that it directly coupled with.
475 This allows us to directly measure the coupling of the Higgs to that quark, unlike the
476 ggF method where the quark in the loop is never directly observed.

477 As we can see, each of these methods has its advantages and disadvantages as well as
478 different valuable information that can be extracted. The result is a need for many
479 different analysis using different techniques to search for each mechanism.

480 **3.2 Parton Distribution Function**

481 The LHC collides protons, however looking at the feynman diagrams in fig. 3.2 we see
482 that it is quarks and gluons (a.k.a partons) that produce these fundamental interactions.
483 This is an indicator that when we calculate the production cross section for a process
484 at the LHC, we have to not only consider the hard-scatter probability of the specific
485 diagram, but also consider the composition of the proton itself. Specifically, we must
486 consider the fraction of the total momentum of the proton held by each of its constituent
487 partons. This concept is described by Parton Distribution Functions (PDFs) which give
488 the probability that the indicated parton carries momentum fraction x of the proton

when probed at with energy scale Q . An example PDF for $Q = 10\text{GeV}^2$ and $Q = 10^4\text{GeV}^2$ in fig. 3.3

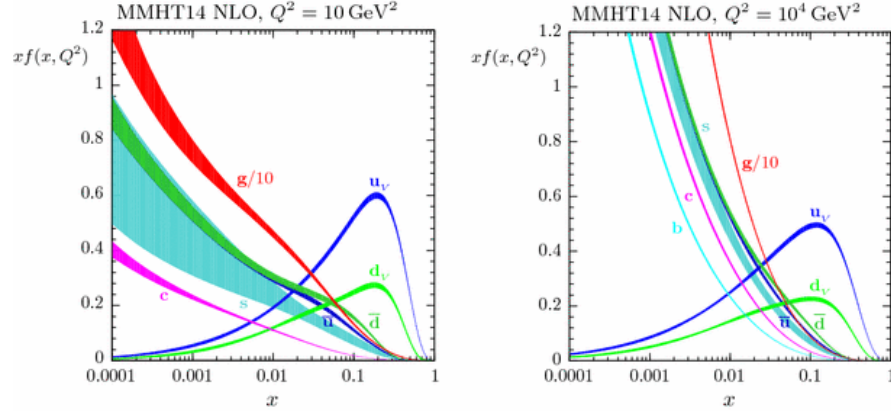


Figure 3.3: [2] MMHT2014 NNLO PDFs at $Q^2 = 10\text{GeV}^2$ and $Q^2 = 10^4\text{GeV}^2$ with associated 68% confidence-level uncertainty bands. The colored regions indicate the probability of finding the labeled parton with a momentum fraction given along the x axis. As expected the u_V and d_V contain the largest fraction of the momentum, however we can also see that many gluons will exist with smaller fractions of the total momentum. Note that as Q^2 increases you are more likely to find something besides a u/d

3.3 Branching Ratios

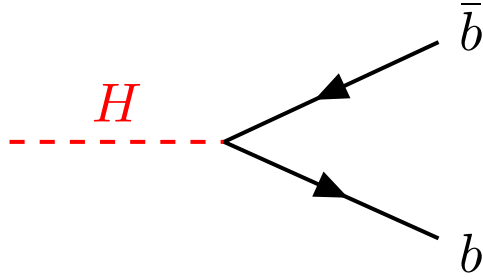
The coupling of the SM Higgs with the gauge bosons and fermions has been shown to give these particles their mass, however it also means that the Higgs can decay into all of these particles. In order of most to least likely final states of a Higgs decay we

495 have the decay to; a pair of b -quarks ($b\bar{b}$), a pair of weak vector bosons where one is
496 off-shell (VV^*), two gluons (gg), a duo of tau leptons ($\tau^+\tau^-$), or a pair of photons ($\gamma\gamma$).
497 Similar to the ggF production mechanism discussed in section 3.1 the decays to massless
498 gauge bosons (photons and gluons) are facilitated through loops of massive particles.
499 The exact feynman diagrams depicting the above process' are shown in fig. 3.4 while
500 information about their branching ratios is detailed in table 3.2.

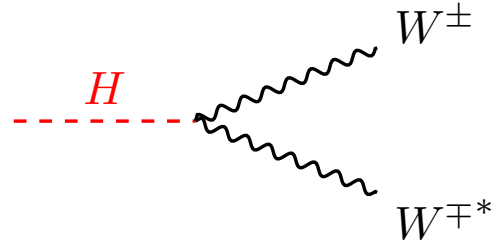
Table 3.2: The branching ratios and the relative uncertainty for a Standard Model Higgs boson with $m_H = 125$ GeV [1].

Decay Channel	Branching Ratio	Relative Uncertainty
$H \rightarrow b\bar{b}$	5.84×10^{-1}	+3.2% -3.3%
$H \rightarrow W^+W^-$	2.14×10^{-1}	+4.3% -4.2%
$H \rightarrow \tau^+\tau^-$	6.27×10^{-2}	+5.7% -5.7%
$H \rightarrow ZZ$	2.62×10^{-2}	+4.3% -4.1%
$H \rightarrow \gamma\gamma$	2.27×10^{-3}	+5.0% -4.9%
$H \rightarrow Z\gamma$	1.53×10^{-3}	+9.0% -8.9%
$H \rightarrow \mu^+\mu^-$	2.18×10^{-4}	+6.0% -5.9%

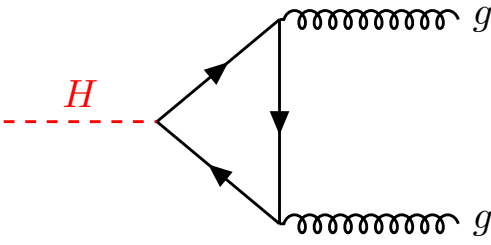
501 In table 3.2 the order is determined by two distinct effects; the proportionality of the
502 Higgs couplings to the mass of the decay product, and whether or not the rest mass
503 of the higgs is sufficient to produce the two final state objects. In fig. 3.5 you can see
504 that as the mass of the higgs boson gets closer to $2m_W$ the cross section for $H \rightarrow WW$
505 grows.



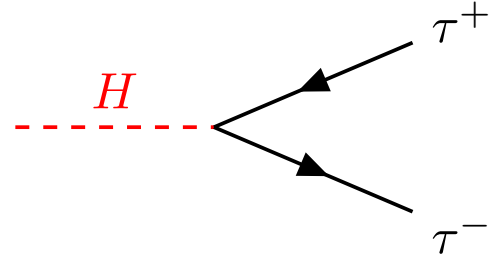
(a) $H \rightarrow b\bar{b}$



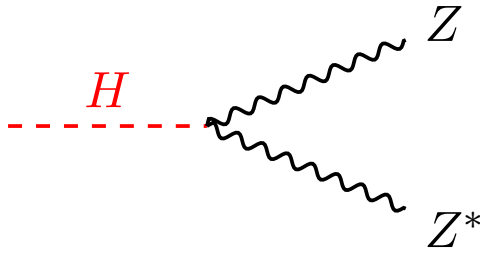
(b) $H \rightarrow W^\pm W^\mp^*$



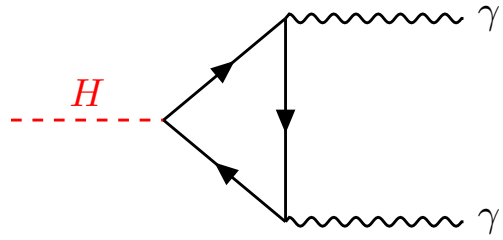
(c) $H \rightarrow gg$



(d) $H \rightarrow \tau^+\tau^-$



(e) $H \rightarrow ZZ^*$



(f) $H \rightarrow \gamma\gamma$

Figure 3.4: Feynman diagrams representing the leading Higgs decay channels.

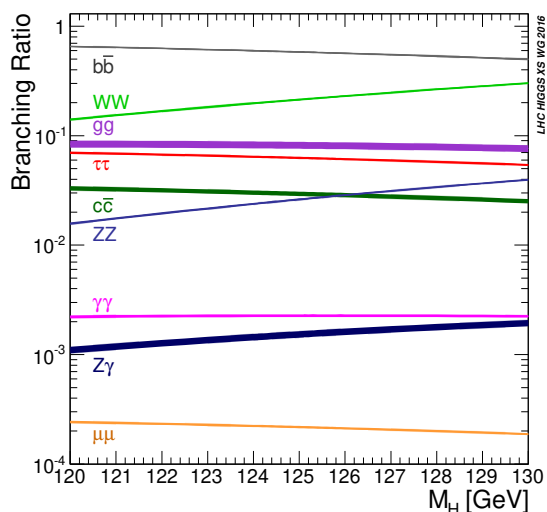


Figure 3.5: Branching ratios for the decay of the SM Higgs boson near $m_H = 125\text{GeV}$ including theoretical uncertainty bands [1]

3.4 Evidence for the SM Higgs

Using the above information about predicted final states the CMS and ATLAS experiment collaborations analyzed 5 fb^{-1} of LHC Run 1 data [3] to make measurements of the SM Higgs production cross-sections and branching ratios. The combined results of these studies can be seen in fig. 3.6 fig. 3.7 and fig. 3.8. Given the uncertainties on the measurements these results show good agreement between the predictions of the Standard Model and experiment with all best fit values falling within 2σ of the SM theoretical prediction.

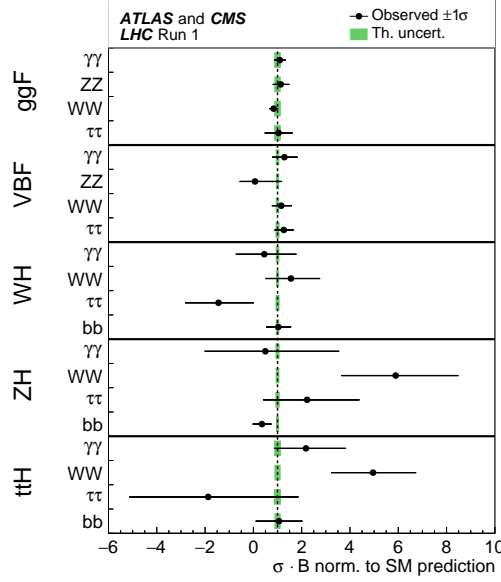


Figure 3.6: Best fit values of $\sigma_i \cdot B^f$ for each specific channel $i \rightarrow H \rightarrow f$, as obtained from the generic parameterisation with 23 parameters for the combination of the ATLAS and CMS measurements. The error bars indicate the 1σ intervals. The fit results are normalised to the SM predictions for the various parameters and the shaded bands indicate the theoretical uncertainties in these predictions. Only 20 parameters are shown because some are either not measured with a meaningful precision, in the case of the $H \rightarrow ZZ$ decay channel for the WH , ZH , and $t\bar{t}H$ production processes, or not measured at all and therefore fixed to their corresponding SM predictions, in the case of the $H \rightarrow b\bar{b}$ decay mode for the ggF and VBF production processes [3].

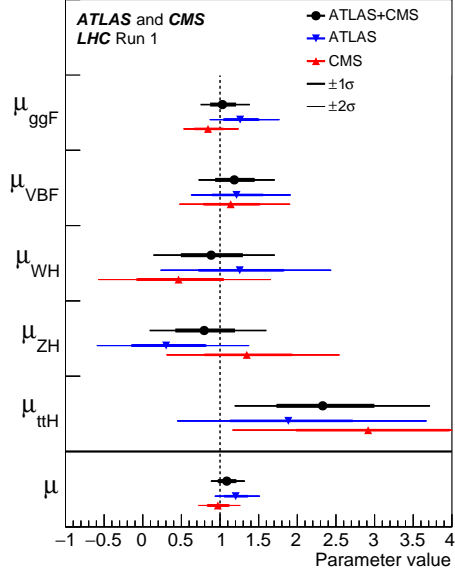


Figure 3.7: Best fit results for the production signal strengths for the combination of ATLAS and CMS data. Also shown are the results from each experiment. The error bars indicate the 1σ (thick lines) and 2σ (thin lines) intervals. The measurements of the global signal strength μ are also shown [3].

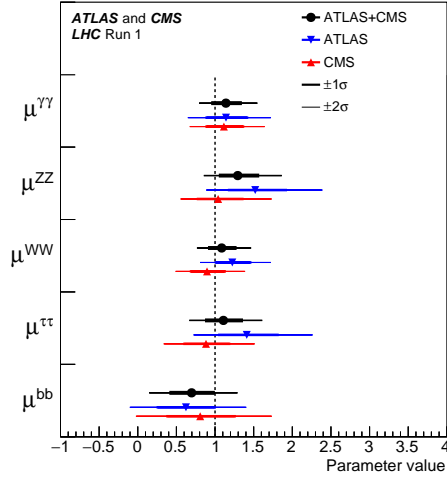


Figure 3.8: Best fit results for the decay signal strengths for the combination of ATLAS and CMS data. Also shown are the results from each experiment. The error bars indicate the 1σ (thick lines) and 2σ (thin lines) intervals [3].

514 3.5 Boosted Higgs

515 The strong agreement between the theoretical predictions of the SM Higgs boson and
516 experiment shown in section 3.4 represents the fulfillment of a generation of incredible
517 technological and theoretical achievement. The next step is to push the search for
518 deviations from the model that might hint at the physics of mysteries like the matter /
519 anti-matter asymmetry of the universe, dark matter, the particle nature of gravity and
520 dark energy. One such avenue for search comes in the transfer of large ammounts of
521 momentum in massive particle loops like that of the ggF Higgs production mechanism.
522 By more accurately measuring the couplling of the Higgs to quarks, we not only increase
523 our confidence in the SM, we are also gain access to this possible new physics. To this

524 end, and for the purposes of suppressing the QCD multijet background, a study of
525 Boosted Higgs production was undertaken and is discussed further in part III.

526

Part II

527

Experimental Apparatus and

528

Associated Facilities

529 Chapter 4

530 The Large Hadron Collider

531 Located 100 meters under the Swiss / French boarder lies the 26.7 kilometer Large
532 Hadron Collider (LHC) [4]. The culmination of a huge international collaboration,
533 this apparatus is used to produce proton and heavy ion collisions for observation by the
534 four major experiments at the LHC: ATLAS, CMS, LHCb, and ALICE. The system was
535 designed for a maximum center-of-mass energy of $\sqrt{s} = 14$ TeV and a peak instantaneous
536 luminosity of $L = 10^{34} \text{cm}^{-2} \text{s}^{-1}$.

537 The first LHC workshop was held in 1984 in Lausanne at the European Organization
538 for Nuclear Reserach (CERN) [5]. The nearly 30 year old case for a machine that
539 would push towards the discovery of the elusive Higgs Boson was presented using the
540 existing CERN accerlerator facilities and the Large Electron Positron (LEP) collider
541 tunnel. The proposal became reality on September 10, 2008 when the first proton beams
542 were circulated, only to have calamity strike 9 days later in the form of a catastrophic

543 electrical fault. The repairs and improvements lasted until November 2009 when the
544 LHC restarted. Since then this modern marvel has worked wonderfully and, as hoped,
545 lead to the discovery of the Higgs Boson by the CMS and ATLAS collaborations July
546 4, 2013.

547 The following chapter provides a brief introduction to the worlds most powerful accel-
548 erator starting with the little red bottle of hydrogen in building XXX, and ending with
549 the interaction point where protons collide at the highest energies ever produced.

550 4.1 Particle Injecton Chain

551 We begin with the most common element in the Universe, hydrogen, as our source of
552 protons. A bottle of hydrogen gas provides 100 microsecond pulses of raw H_2 which
553 is then injected into a Duoplasmatron. There, a strong electric field and free elctrons
554 from a cathode ionize the molecule into bare H^+ aka a proton! These protons are
555 then accelerated by a 90kV field, leaving the Duoplasmatron with 1.4% speed of light
556 ($\sim 4000\text{km/s}$) or, in relativistic units, about 83KeV. The bare protons are then fed
557 into the accelerating RadioFrequency (RF) cavities of Linear Accelerator 2 (LINAC2).
558 Inside, conductors charged by a powerful oscillating electromagnetic field accelerate the
559 protons resulting in a 50MeV energy. Along the way, small quadrupole magnets shape
560 the proton packet insuring they remain in a tight beam. This pattern of accleration
561 with RF cavities and shaping/turnig with magnets is then repeated with CERN's first

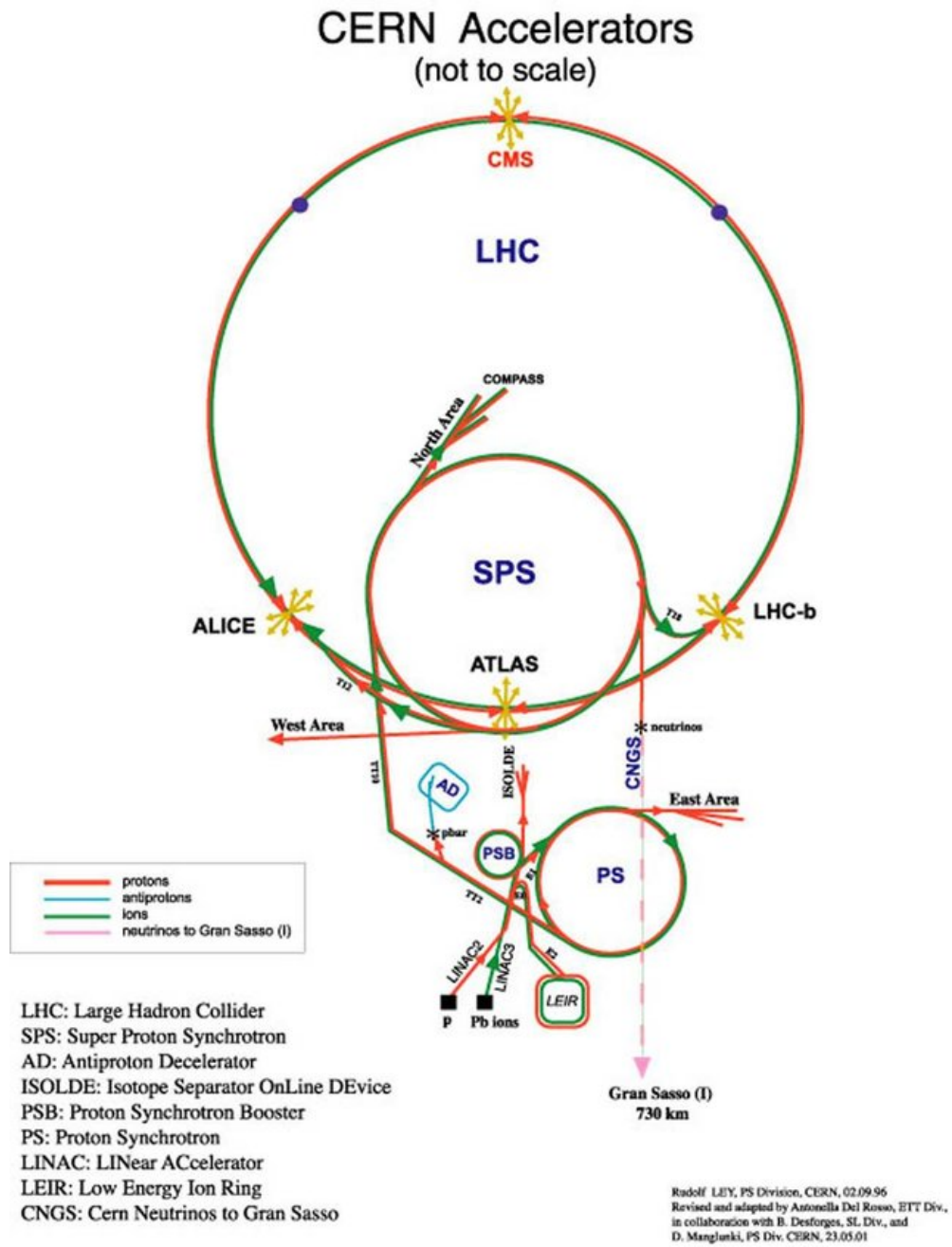


Figure 4.1: CERN accelerator complex

562 synchrotron, the Proton Synchrotron (PS) rendering a 1.4 GeV beam. The final step
563 before the LHC comes with the Super Proton Synchrotron where the same technologies
564 are implemented to produce 450 GeV protons, ready for injection into the LHC. A
565 diagrammatic representation of this chain can be seen in fig. 4.1

566 In order to produce proton-proton collisions the LHC uses two beams circulating in
567 opposite directions. The beams are not continuous, but instead consist of bunches, or
568 buckets, of $\mathcal{O}(10^{11})$ protons with a spacing of 25ns. Given the LHC circumference this
569 allows for 3564 buckets, however only 2808 are filled per beam due to safety requirements
570 and injection limitations. Each beam takes 4 minutes and 20 seconds to fill and then an
571 additional 20 minutes to for the protons to reach their maximum energy of 7 TeV TeV,
572 or 99.99999991% the speed of light! Under normal operating conditions these beams
573 can be used for many hours.

574 4.2 LHC layout and design

575 While often depicted as a perfect circle the LHC is in reality an octagon with rounded
576 edges, called arcs, as can be seen in fig. 4.2. Here you can see the counter circulating
577 beams of protons depicted in red and blue. These beams are focused and collided at
578 the 4 dedicated interaction points at rates of up to 40 MHz. Two of these points are
579 occupied by the ATLAS and CMS experiments, both of which are high luminosity,
580 multi-purposed experiments.

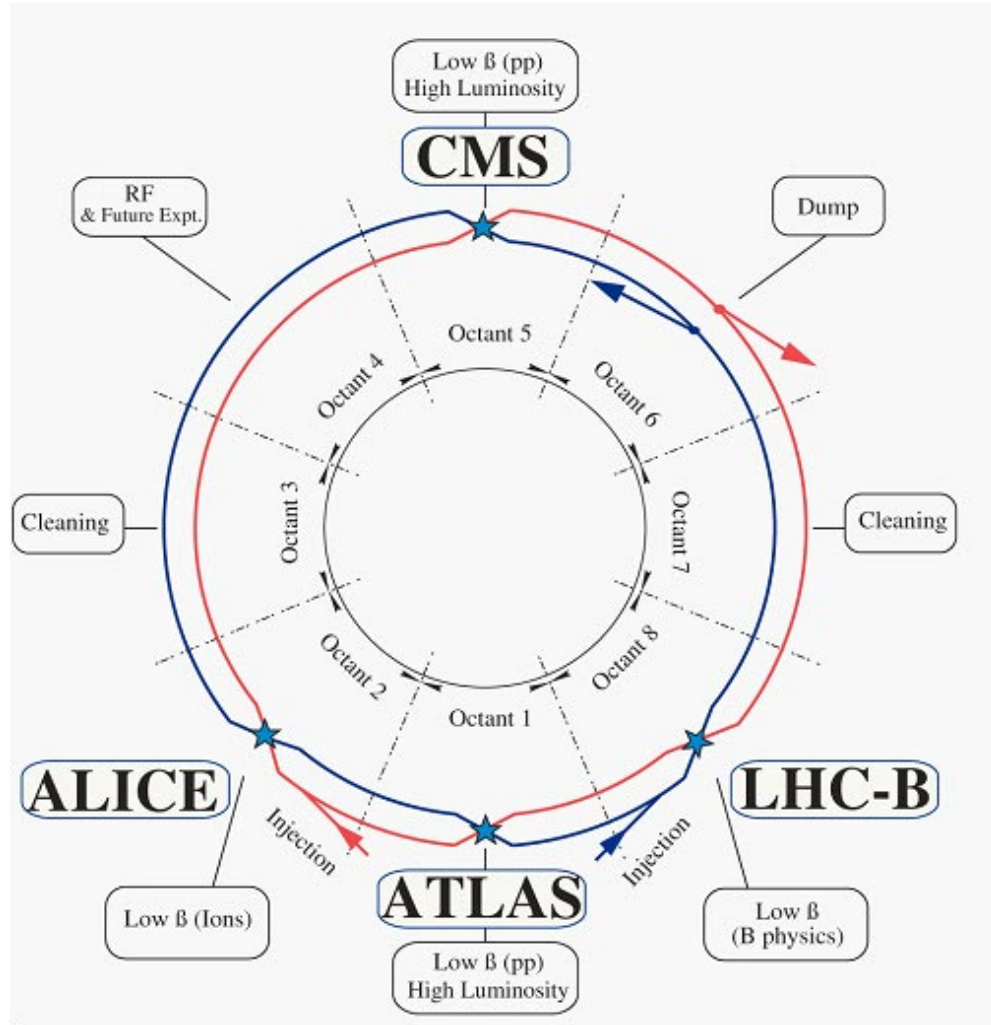


Figure 4.2: Labeled diagram of all the experiments at the LHC indicating the counter circulating beams and points of interest along the circumference of the accelerator.

581 The exact design of the tunnel is due to the experimental constraints of the original
 582 machine for which it was built, the Large Electron Positron (LEP) Collider. For the
 583 $\sim 2,000$ times lighter electron the maximum energy was limited by the synchrotron
 584 radiation, proportional to $\frac{1}{m^4}$, requiring long straight sections of accelerating RF cavities
 585 to recouperate the lost energy. Given that this effect is $\mathcal{O}(10^{13})$ times smaller for the
 586 proton the LHC is instead limited by our ability to design and construct magnets strong
 587 enough to bend the beam given the already determined curvature of the 8 arcs.

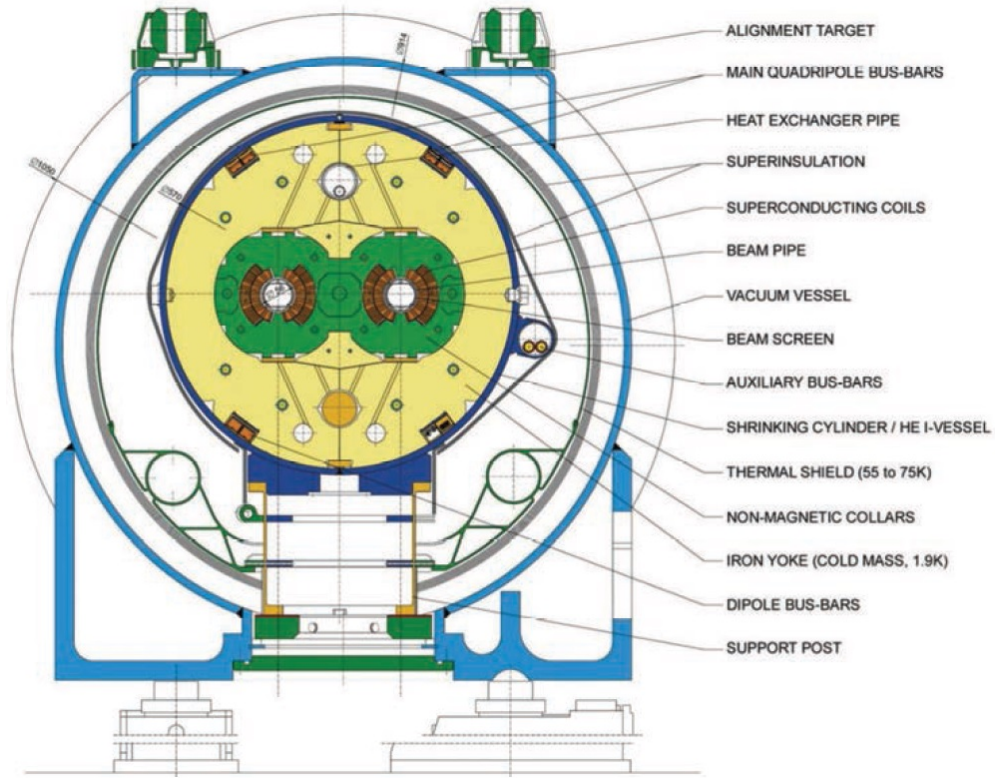


Figure 4.3: Depiction of a LHC dipole magnet 2-in-1 design labeling the major components

588 The oppositely circulating beams must each have their own ring and magnetic field
589 which lead to the creation of a twin-bore (i.e. "two-in-one") magnet design, a cross
590 section of which can be seen in fig. 4.3. These magnets are constructed using NbTi
591 superconductors which are cooled to 2K using superfluid helium. These magnets are
592 designed to provide the needed 8.33 T magnetic field required to bend the beams at the
593 design beam energy of 7 TeV. In total 1231 of these 15 m long bending dipole magnets
594 are used, in association with 392 5-7m long quadrupole magnets which are responsible
595 for keeping the proton bunches in a tight beam by squeezing them either horizontally
596 or vertically.

597 **4.3 Performance**

598 Since the begining of its stable running in 2010 the LHC has performed well, even
599 exceeding our expectations. While the experiment itself is incredibly complex, the
600 performance of the machine, for the purposes of our analysis, can be reduced to two
601 numbers; the familiar center of mass energy of the beams and a less common quantity
602 known as the integrated luminosity.

603 For particle physics the integrated luminosity is proportional to the total number of
604 collisions recorded during a specified time period, while the instantaneous luminosity is
605 proportional to the bunch crossing rate along with the cross section of a proton-proton
606 interaction and represents the potential number of collisions per second. Knowing this

607 we can see that the integrated luminosity, L_{int} is simply the integral of the instantaneous
608 luminosity $L_{inst.}$ for a choosen data period as seen in eq. (4.1).

$$L_{int} = \int L_{inst.} dt \quad (4.1)$$

609 For a standard Gaussian beam, $L_{inst.}$ can be written as

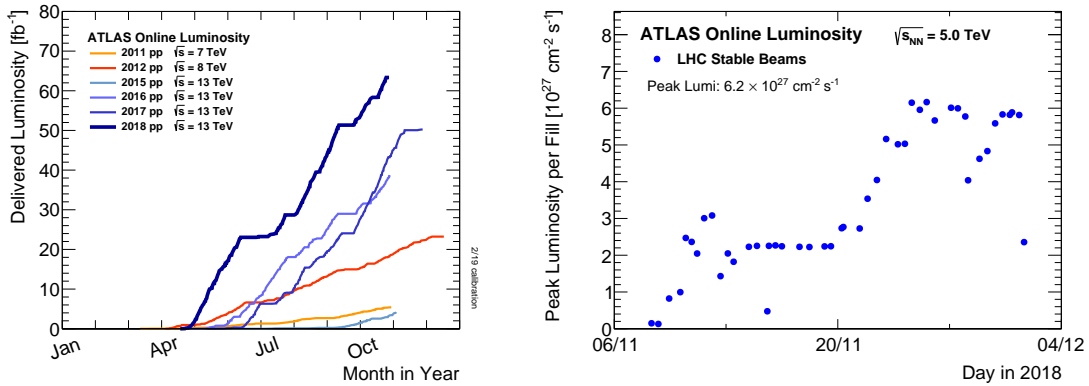
$$L = \frac{N_b^2 n_b f_{rev} \gamma_r}{4\pi \epsilon_n \beta^*} F \quad (4.2)$$

610 where N_b is the number of particles per bunch, n_b the number of bunches per beam,
611 f_{rev} the revolution frequency, γ_r the relativistic gamma factor, ϵ_n the normalized trans-
612 verse beam emittance, β^* the beta function at the collision point, and F the geometric
613 luminosity reduction factor due to the crossing angle at the interaction point given by

$$F = \left(1 + \left(\frac{\theta_c \sigma_z}{2\sigma^*} \right)^2 \right)^{-1/2} \quad (4.3)$$

614 where θ_c is the full crossing angle at the interaction point, σ_z is the RMS bunch length,
615 and σ^* is the transverse RMS beam size at the interaction point.

616 For the ATLAS experiment the integrated luminosity for each year can be seen in
617 fig. 4.4a as well as an example of the instantaneous luminosity for the choosen year in
618 fig. 4.4b.



(a) Integrated Luminosity 2011 - 2018 (b) 2018 Peak Instantaneous Luminosity

Figure 4.4: Luminosity is monitored as both a running total known as the Integrated Luminosity as depicted in (a) and as an instantaneous quantity as shown in (b)

619 4.4 Pile-up at the LHC

620 Given the large number of protons per bunch and the cross-section of a proton-proton
 621 interaction, the probability to observe multiple interactions per bunch crossing is quite
 622 high. These multiple-interaction are known as pile-up, μ or the time averaged represen-
 623 tation $\langle\mu\rangle$, and come in two different forms:

- 624 1. **In-time pile-up:** These are the other proton-proton collisions that occur during
 625 the same bunch crossing as the primary interaction that caused the Data Acquisition (DAQ) system to trigger. These are the standard extra interactions we expect
 626 to observe as stated above.
 627
- 628 2. **Out-of-time pile-up:** These are interactions that occur either before or after a

629 bunch crossing that causes the DAQ to trigger. This effect is generally due to the
 630 long integration times of some detector electronics.

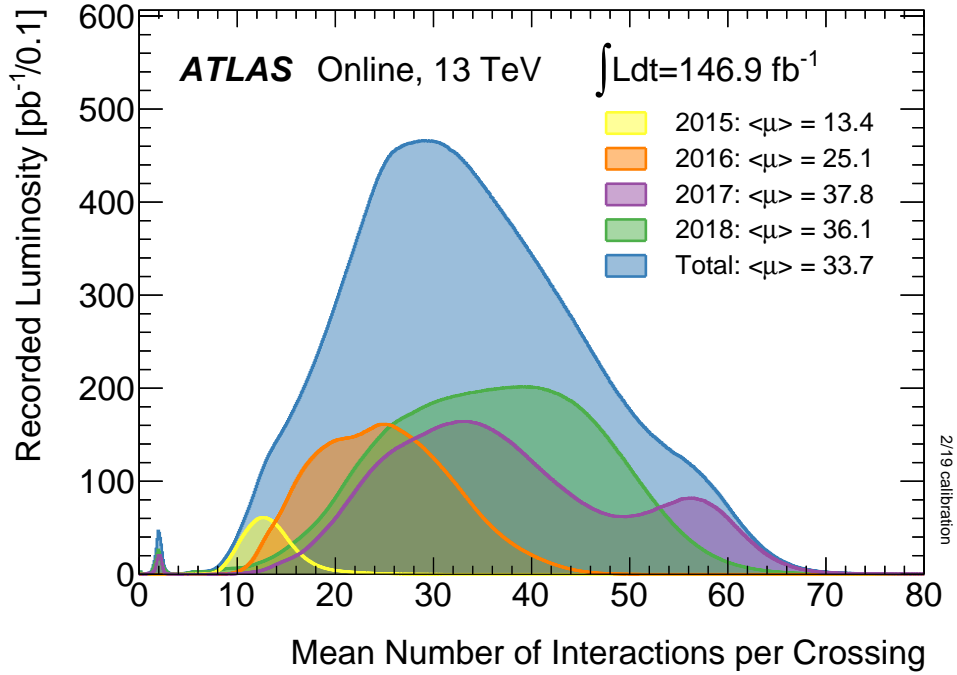


Figure 4.5: Pileup for data taking periods 2015 - 2018

631 The pile-up profile for past years can be seen in fig. 4.5. The width of this distributino
 632 is due a combination of Poissonian statistics, the decrease in number of protons per
 633 bunch over the lifetime of a single run, and optimization tweaks to the beam's profile
 634 during runtime. Understanding and eliminating the noise from these pile-up events is
 635 crucial to reconstructing physics variables to represent the primary interaction we hope
 636 to observe.

637 Chapter 5

638 The ATLAS Detector

639 Given the immense energies available at the LHC, and the veritable zoo of particles we
640 are trying to detect, we require a general-purpose experiment in order to fully exploit
641 the full range of physics opportunities provided. Two international collaborations rose
642 to this challenge, the CMS (Compact Muon Solenoid) and ATLAS (A Torroidal LHC
643 ApparatuS) experiments. While both have similar physics goals and each of them
644 strengths and weaknesses, this dissertation will focus on the ATLAS experiment and
645 the intricacies of its three main sub-detectors and two massive magnet systems depicted
646 in fig. 5.1.

647 Originally proposed in 1994 the ATLAS experiment was completed in 2008. On July
648 4th, 2012 in a joint announcement the ATLAS and CMS experiments announced the
649 discovery of the long predicted Higgs Boson. The collaboration now boasts over 3000
650 physicists from 175 institutions spread across 38 countries and continues to probe

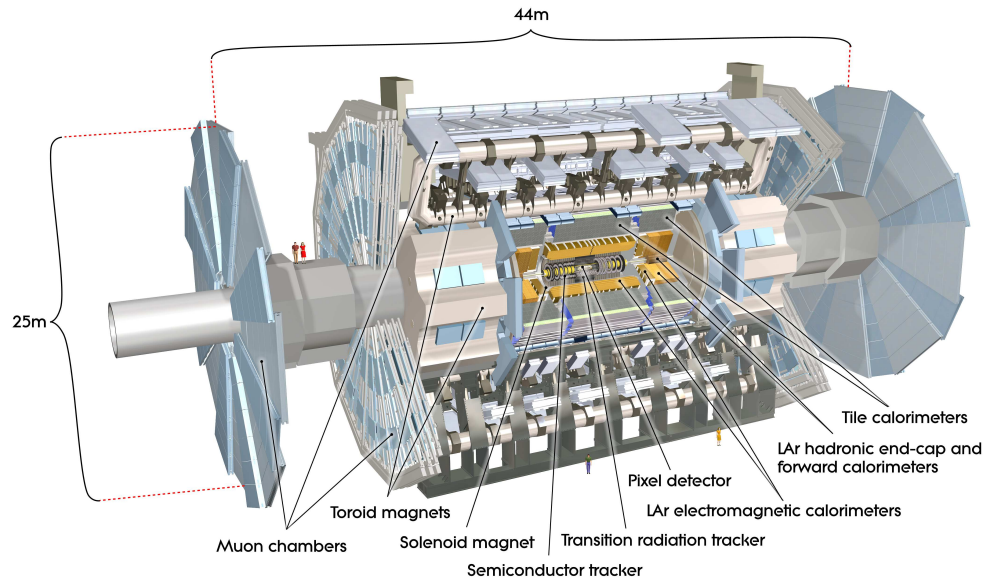


Figure 5.1: [6] Here we see a cut-away side view of the ATLAS detector with the major components labeled. Note that within each of these labeled components there may exist multiple different detector technologies. For scale two people in red are shown standing between the disk muon chambers on the left side of the figure.

651 the limits of the Standard Model in pursuit of answers to some of Humanities deepest
652 questions.

653 Located approximately 100 meters underground in a vast excavated chamber, the AT-
654 LAS detector rests its 7000 metric tonnes on a bed of concrete reinforced steel. Out of
655 it flows the signals of over 100 million electronic channels through a zip tied mass of
656 greater than 3000 kilometers of cabling. At its very center is one of the four interaction
657 points of the LHC, specifically Point 1, where the two counter circulating proton beams
658 are skillfully shaped and then collided by a series of magnets. The energetic particles
659 resultant from this collision then fly out in all directions into the bulk of the ATLAS
660 detector.

661 The first sub-system they meet is the Inner Detector (ID) and its many layers of strip
662 and pixel silicon detectors along with a transition radiation gaseous wire detector, all
663 bathed in the 2T magnetic field of the surrounding superconducting solenoidal magnet.
664 This system exploits the ionization of charged particles to track their curved trajectory
665 through the magnetic field. This curvature gives us charge information, a momentum
666 measurement, and precision 3D vertices crucial to the identification of the secondary
667 vertices of a b-hadron decay.

668 Outside of the solenoid the particles are faced with first the Electromagnetic and then
669 the Hadronic sampling calorimeters. Here, layers of scintillator and high radiation length
670 materials are implemented to measure the energy of electrons, photons, and hadrons.
671 As the goal is to completely absorb the energy of all outgoing particles the calorimeter

672 has a nearly 4π solid angle coverage.

673 Finally we have the muon system surrounding the calorimeter and equipped with its
674 own torroidal magnet system. Here the charged muon bends in the magnetic field
675 while leaving a trail of ionization in the muon spectrometer before exiting the detector
676 completely. Neutrinos are the only other standard model particle that leave the detector,
677 however they do so without detection. A depiction of the various particle interactions
678 with the different detector sub-systems can be seen in fig. 5.2

679 In the following sections I will explain our choosen coordinate system and give a more
680 detailed reveiw of these 3 detector sub-systems.

681 5.1 ATLAS Coordinate System

682 Using the nominal interaction point as the origin, ATLAS uses a right handed coor-
683 dinate system where the positive x -axis points towards the center of the LHC ring,
684 the positive y -axis points upwards, and the positive z -axis is defined by the counter
685 clockwise circulating beam direction as viewed from above shown in fig. 5.3 [6].

686 Using these coordinates we can define the physical momentum of the objects measured
687 as $\vec{p} = (p_T, p_z)$ with p_T being the momentum of the object in the transverse plane and
688 p_z the momentum along the beam axis. Given the cylindrical symmetry of ATLAS it
689 is desireable to define the polar angle θ from the beam axis with the $r - \phi$ plane being
690 perpendicular to that axis. Since the particles we observe are relativistically boosted

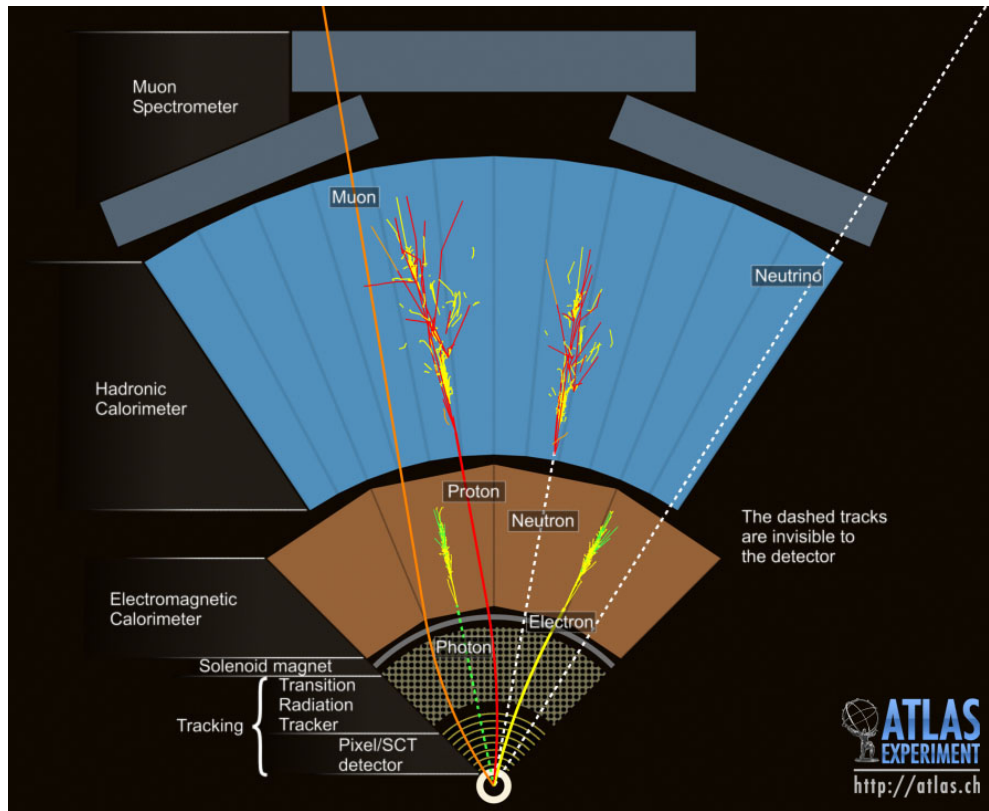


Figure 5.2: This slice of the ATLAS detector depicts how different particles interact with each component of the detector it crosses. A dashed line indicates no interaction while a solid line indicates interaction. Electrons (yellow/green) and charged hadrons (red) interact with the tracker and curve in the solenoid's magnetic field. Electrons and photons (yellow/green) are absorbed by the Electromagnetic calorimeter. All hadrons (red/yellow) are absorbed by the Hadronic calorimeter. The muons (orange) curve in both the solenoid and torroid magnetic fields before exiting the detector. Finally, the neutrinos (white) pass through the entire detector without interacting.

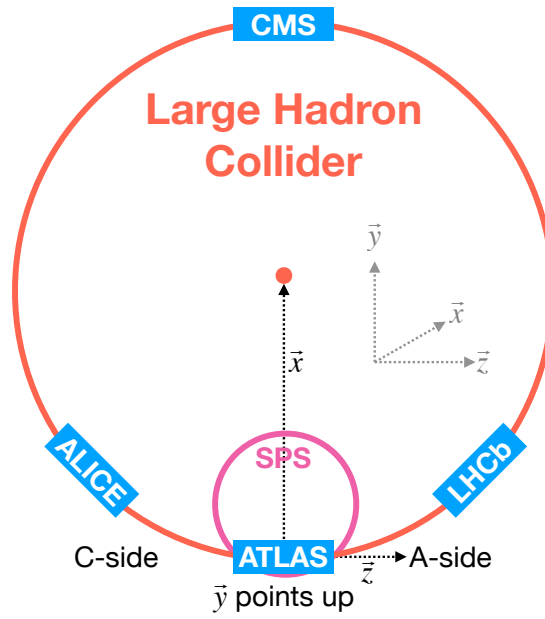


Figure 5.3: [7] A cartoon view of the the LHC from above showing the SPS, LHC and the four main experiments of the LHC: ATLAS, CMS, LHCb, and ALICE. The standard cartesian coordinate system is shown with its origin at the ATLAS interaction point, the positive x -axis towards the center of the LHC, the positive y -axis pointing upwards, and the positive z -axis pointing along the beamline towards the "A-side"

691 in the z -axis it is desirable to use the Lorentz invariant quantity pseudorapidity (η)
 692 defined in terms of the polar angle by

$$\eta = -\ln \tan \left(\frac{\theta}{2} \right). \quad (5.1)$$

693 where $\eta = 0$ is in the $x - y$ plane and larger values of $|\eta|$ being closer to the beam axis
 694 as can be seen in fig. 5.4.

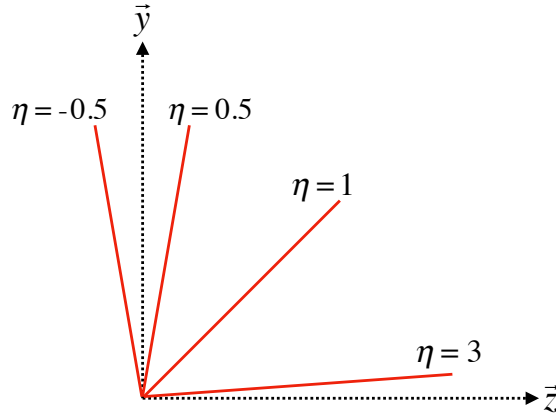


Figure 5.4: Modified from [7] this cartoon represents a selection of pseudorapidity (η) values overlaid with some cartesian coordinates (dashed black lines). The redlines are drawn for $\eta = \pm 0.5, 1.0, 3.0$

695 In this analysis the angular separation between objects in the detector is calculated and
 696 represented using the geometric quantity

$$\Delta R = \sqrt{(\Delta\eta)^2 + (\Delta\phi)^2} \quad (5.2)$$

5.2 Tracking with the Inner Detector

With its closest component, the insertable b-layer (IBL) [8], only 3.3 cm from the interaction point The Inner Detector (ID), shown in fig. 5.5 [9, 10], faces the incredible challenge of providing precision momentum resolution and identification of both primary and secondary vertex measurements of charged tracks all while receiving the highest fluence.

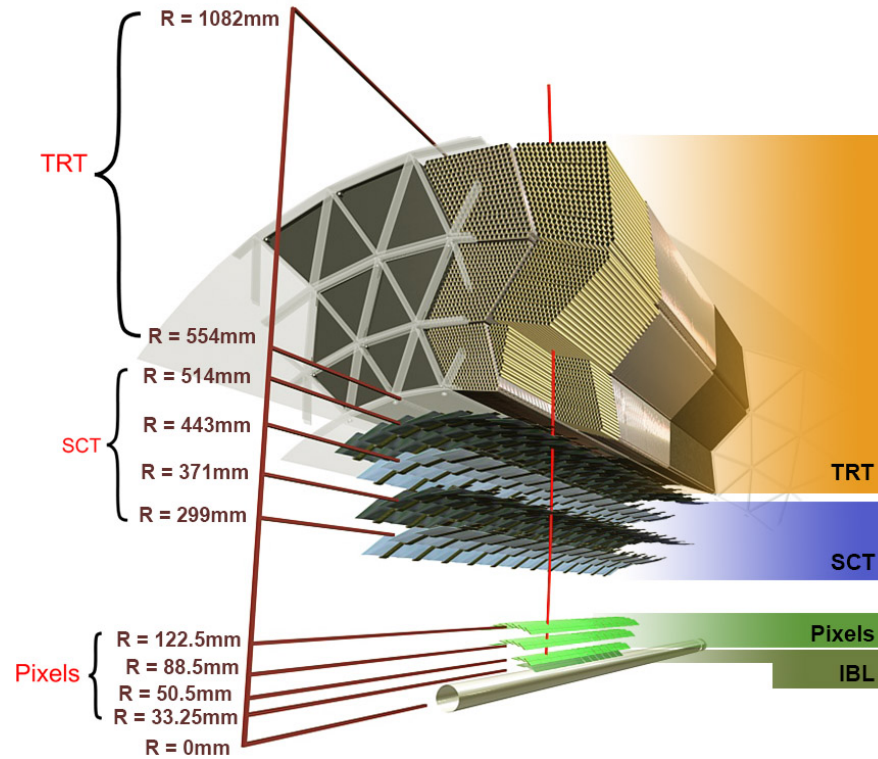


Figure 5.5: [8] Diagram of inner detector

It is designed to be very compact to reduce the probability of a particle decaying inside and to give precision measurements of the particles curvature in the 2T solenoidal

705 magnetic field. This leads to excellent momentum resolution above the nominal p_T
 706 threshold of 0.5 GeV and within the pseudorapidity range of $|\eta| < 2.5$ as shown in
 707 fig. 5.6

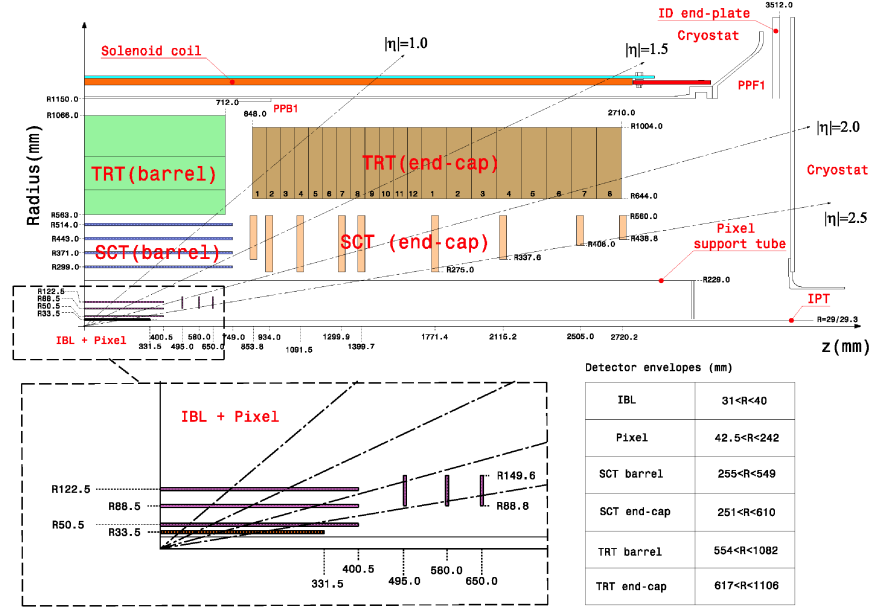


Figure 5.6: [11] Schematic of the Inner Detector including eta lines. Each component shown is cylindrically symmetric leading to a multi-layered detector.

708 The ID is composed of three different detector technologies for particle trajectory re-
 709 construction: The Pixel Detector, Semiconductor Tracker (SCT) and the Transition
 710 Radiation Tracker (TRT). These will be discussed in the following sections.

711 5.2.1 Pixel Detector

712 The ATLAS Pixel Detector [6], the innermost subdetector of the ID, is designed to
713 give the best resolution possible as close as possible to the interaction point. This is
714 accomplished using the 4 barrel layers and the 3 disks per endcap as indicated in fig. 5.6.
715 The inner most barrel layer, the IBL, has pixel dimensions of $50\mu\text{m}(\hat{\phi}) \times 250\mu\text{m}(\hat{z}) \times$
716 $200\mu\text{m}(\hat{r})$. For the other layers the dimensions are $50\mu\text{m}(\hat{\phi}) \times 400\mu\text{m}(\hat{z})$ for about 90%
717 of the pixels and $50\mu\text{m}(\hat{\phi}) \times 600\mu\text{m}(\hat{z})$ for the others, all with a thickness of $250\mu\text{m}(\hat{r})$.
718 This gives a total active area of 1.88m^2 collected through 92.4 million readout channels,
719 more than half of the total number of channels for ATLAS. This detailed charged particle
720 information very close to the interaction point is crucial not only for pattern recognition
721 for track reconstruction, but also for the reconstruction of the primary and secondary
722 vertices intrinsic to the decay of a b -hadrons, a critical element of the analysis presented
723 in this thesis.

724 5.2.2 Semiconductor Tracker

725 Encompassing the Pixel Detector, the Semiconductor Tracker (SCT) [6] is composed of
726 double sided silicon microstrips modules. Each side of the 4088 modules is constructed
727 out of two silicon strip sensors that are daisy chained together. The result is 768
728 composite strips each 12.6cm with an inter-strip pitch of $80\mu\text{m}$. In the barrel the strips
729 are aligned with the \hat{z} direction, while in the end caps they are aligned with the \hat{r}
730 direction. In both cases the separation of the strips is constant in $\hat{\phi}$. The two sides are

731 rotated with respect to each other by $40\mu\text{m}$ to allow for position measurement along the
 732 length of the strip. These modules are then used to tile the 4 barrel layers and 9 disks
 733 per endcap (18 disks in total) as seen in fig. 5.6. This design is chosen to ensure that
 734 each charged track interacts with 8 strip layers (equivalent to four space points). This
 735 information is used to further measure the momentum and impact parameter, and as
 736 well as vertex identification of charged particles.

737 **5.2.3 Transition Radiation Tracker**

738 The Transition Radiation Tracker [6], the outermost subdetector of the ID, provides
 739 tracking through the detection of transition radiation from ultra-relativistic charged
 740 particles for $\eta < 2.0$ using 350,000 drift tube channels also known as straws. The 4mm
 741 diameter straws are filled with a 70% Xe, 27% CO₂, and 3% O₂ gas mixture and a $31\mu\text{m}$
 742 diameter gold-plated tungsten wire anode at the center for the collection of the ionization
 743 signal. In the barrel 73 azimuthally symmetric layers of 144cm straws are oriented parallel
 744 to the beam pipe with an electrical division in the center of each allowing the two sides
 745 to be read out separately. For each endcap the straws are radially oriented in 160
 746 symmetric planes each containing 768 37cm long drift tubes shown in fig. 5.6. In both
 747 the barrel and the end caps polypropylene fibers (barrel) or foils (encaps) function as the
 748 transition radiation material which causes the relativistic charged particles to radiate
 749 and thus ionize the gas in the straw. The amount of transition radiation produced
 750 is proportional to the Lorentz factor meaning that lighter particles (e.g. electrons) will

751 produce more radiation. Thus, by defining a high and low threshold, we can identify
 752 tracks belonging to electrons by requiring they register more high-threshold hits. There
 753 are typically 36 TRT hits per charged track.

754 5.3 Calorimetry

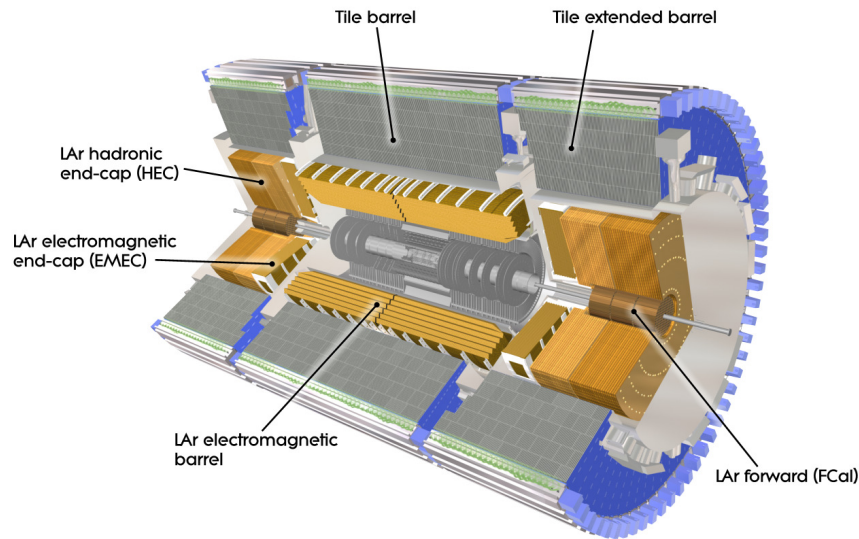


Figure 5.7: [6] A cutaway diagram of ATLAS's sampling calorimeters

755 Once the proton collision remnants have passed through the ID and it's surrounding
 756 solenoid they enter into the ATLAS calorimeters depicted in fig. 5.7. Sampling calorime-
 757 ter technologies were choosen for their compact geometry and lower cost point. These
 758 are constructed by alternating layers of absorber, a dense material which reduces the
 759 incedent particles energy, and active material which produces a detectible signal when
 760 a partilce passes through. This means that the detected signal is only a fraction of the

total energy of the particle and thus requires a study of the calorimeter response for calibration purposes [12]. The first system, the Electromagnetic Calorimeter (EMC), is designed to measure the energy of electrons and photons which primarily lose their energy via bremsstrahlung and pair production electromagnetic interactions. Outside of the EMC is the Hadronic Calorimeter (HC) which is designed to measure the energy of jets of hadrons through their electromagnetic and strong interactions. These detectors cover the entire $|\eta| < 4.9$ range and provide complete containment of both Electromagnetic and Hadronic showers with higher granularity in the EMC for $|\eta| < 2.5$, the region matched to the ID, for precision measurements of electrons and photons. By instrumenting this huge space in $|\eta|$ we can search for events with asymmetric energy deposits which imply the existence of a particle we didn't detect represented by missing transverse energy E_T^{miss} .

5.3.1 Electromagnetic Calorimeter

The innermost calorimeter, the Liquid Argon (LAr) Electromagnetic Calorimeter (EMC) [6], uses lead as the absorber and liquid argon as the active material in an "accordion geometry" as seen in fig. 5.8. This geometry was chosen for uniform coverage in $\hat{\phi}$ due to its lack of un-instrumented cracks in the radial direction. The barrel region covers $|\eta| < 1.475$ and an end cap on each side covers $1.375 < |\eta| < 3.2$ each housed in their own cryostat. The barrel is composed of two half barrels with a 4mm gap at $z = 0$ and both end caps are divided into an inner wheel covering $2.5 < |\eta| < 3.2$ and an outer

781 wheel covering $1.375 < |\eta| < 2.5$.

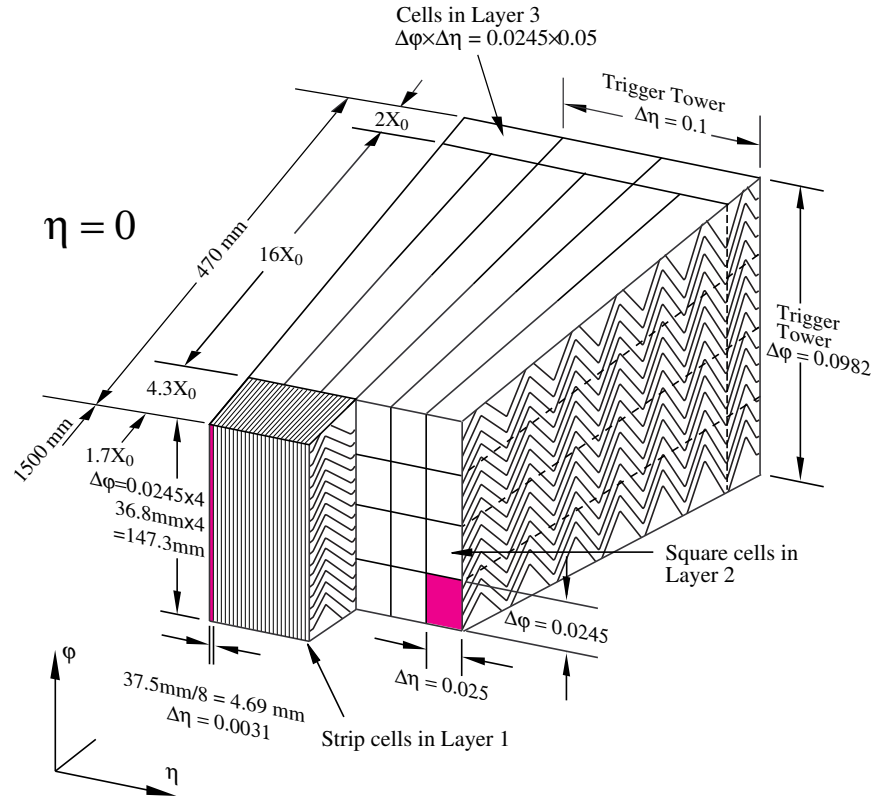


Figure 5.8: [6] Sketch of LAr EMC barrel module where the lead and liquid argon layers are visible in an accordion like geometry. Looking from the foreground to the back there are 3 different types of cells visible.

782 In the $|\eta| < 2.5$ region the EMC has 3 radial layers for precision physics measure-
 783 ments. Layer 1 consists of strip cells which are finely segmented with $\Delta\eta = 0.0031$
 784 and $\Delta\phi = 0.0245$ allowing for precision position resolution which gives discrimination
 785 power between a single γ deposit and the π^0 characteristic $\gamma\gamma$ deposit. Layer 2 , which
 786 collects the largest fraction of energy from electromagnetic shower, is segmented with

787 $\Delta\eta = .025$ and $\Delta\phi = 0.0245$. Layer 3 collects the tail of the electromagnetic shower
 788 using a coarser segmentation of $\Delta\eta = .05$ and $\Delta\phi = 0.0245$. Additionally, in the region
 789 $|\eta| < 1.8$ a thin pre-sampler, which contains no lead absorber, was placed in front of
 790 Layer 1 to allow for energy corrections due to losses upstream of the EMC. Combined
 791 the EMC is > 22 radiation lengths (X_0) in the barrel and $> 24 X_0$ in the end-caps,
 792 where a radiation length is the average distance an electron travels in a given material
 793 before losing $1/e$ of its original energy E_0 via bremsstrahlung radiation.

794 5.3.2 Hadronic Calorimeter

795 Directly outside the EMC envelope is the Hadronic Calorimeter (HC) system [6] which
 796 consists of three sampling calorimeter technologies: the Tile calorimeter, the LAr hadronic
 797 end-cap calorimeter (HEC) and the LAr forward calorimeter (FCal). Combined, these
 798 three subsystems give measurements of hadronic jet energies in the $0 < |\eta| < 4.9$ range.
 799 The tile calorimeter uses steel as the absorber layer and scintillating tiles as the active
 800 material and covers the region $|\eta| < 1.7$ with a barrel section flanked by two barrel ex-
 801 tensions each divided azimuthally into 64 modules. These scintillator tiles are read out
 802 on two sides by wave-length shifting fibers connected to photomultiplier tubes as seen
 803 in fig. 5.9. At $\eta = 0$ the total tile calorimeter thickness is 9.7 nuclear interaction lengths
 804 (λ), where λ is the average distance a hadron travels before interacting inelastically
 805 with a nucleus.

806 The HEC is composed of two independent wheels per end-cap located just past the

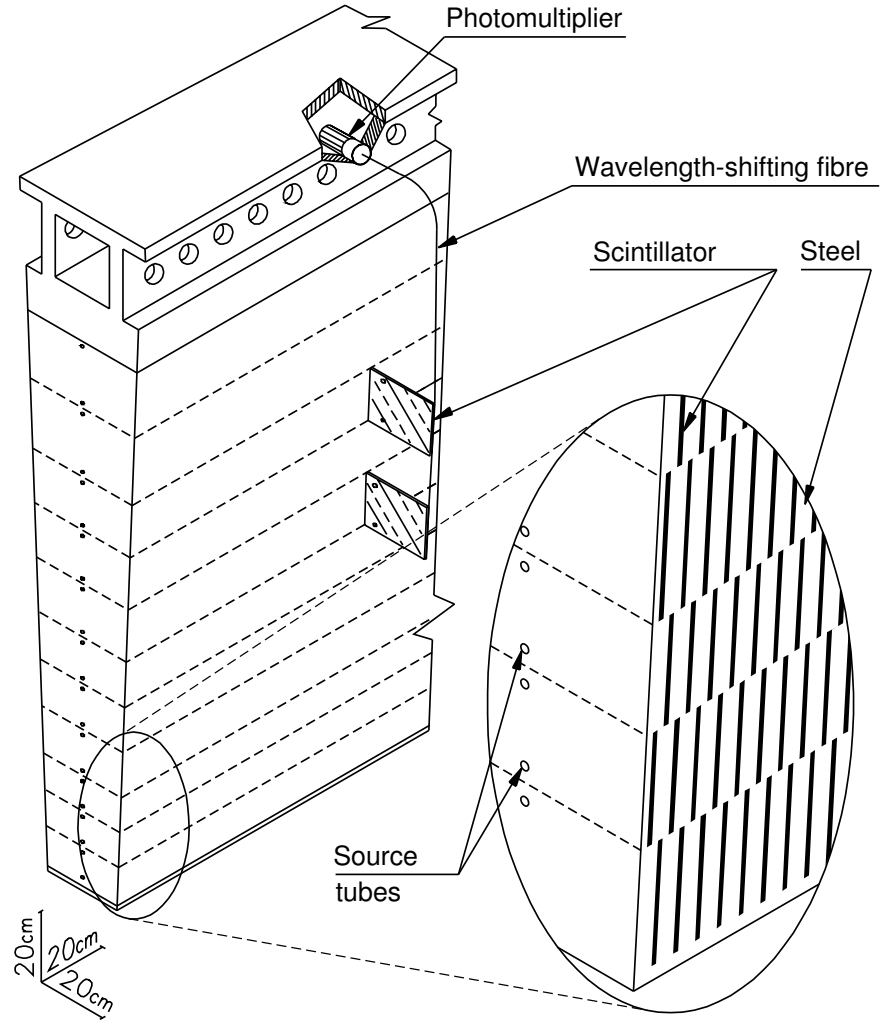


Figure 5.9: [6] Schematic of a tile calorimeter module including a depiction of the connection between the scintillator tile to the photomultiplier via a wavelength-shifting fibre.

807 EMC end-cap but sharing the same cryostat. This system uses copper as an absorber
808 and liquid argon for the active material and covers the $1.5 < |\eta| < 3.2$ range using
809 32 wdg-shaped modules per wheel. Finally, the FCal shares the same cryostat as the
810 EMC and HEC end-caps and acts to extend the coverage of the combined calorimeter
811 system to include the $3.1 < |\eta| < 4.9$ range. Each endcap contains 3 modules, the first
812 an electromagnetic module (Copper/Liquid-Argon) which is followed by two hadronic
813 modules which use (Tungsten/Liquid-Argon).

814 **5.4 Muon Spectrometer**

815 The ATLAS Muon Spectrometer (MS) [6], see fig. 5.10, accomplishes tracking of charged
816 particles in the $|\eta| < 2.7$ region for momentum reconstruction while also providing
817 triggering on charged particles in the $|\eta| < 2.4$ region. The magnetic field necessary for
818 momentum reconstruction is provided by 3 air core torroid systems, one barrel torroid
819 covering $|\eta| < 1.4$ and two endcap torroid systems which are inserted into the inner
820 radius of the the barrel torroid to cover the $1.6 < |\eta| < 2.7$. The so called transition
821 region $1.4 < |\eta| < 1.6$ between these two magnet systems is covered by a combination
822 of the barrel and endcap torroid magnets. Similar to the ID the resolution is inversely
823 proportional to the particle's incident momentum. Any muon with pT lower than 3GeV
824 will never make it to the MS and thus will not be detected.

825 Precision tracking measurements for momentum reconstruction is accomplished using

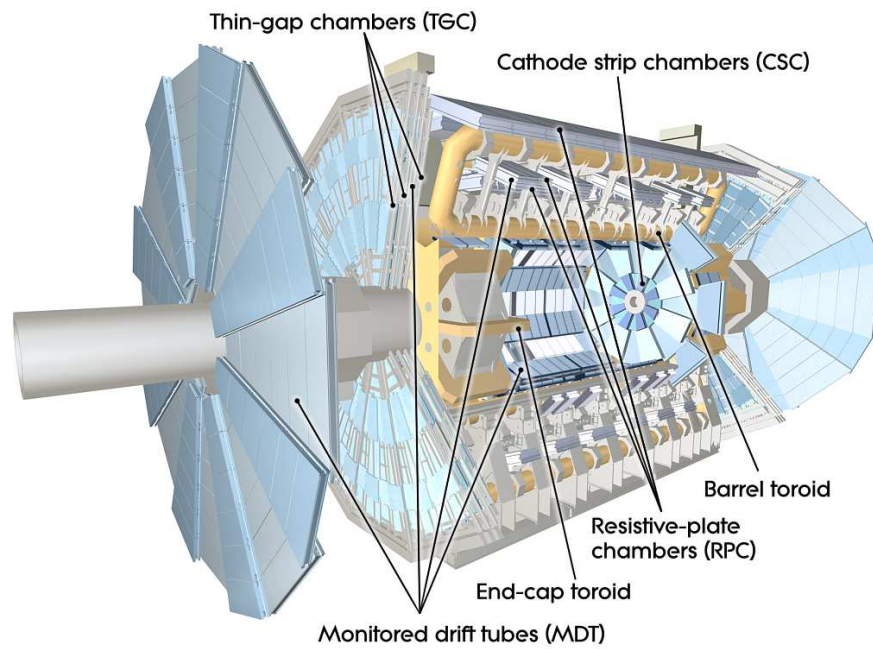


Figure 5.10: [6] A cut-away diagram of the ATLAS muon system and its many sub-detectors.

826 the Monitored Drift Tube chambers (MDTs) for $|\eta| < 2.0$ and using Cathode-Strip
827 Chambers (CSCs) for $2.0 < |\eta| < 2.7$. The MDT system consists of 1163 drift tube
828 chambers arranged in three to eight layers for varying η . The CSCs are designed to
829 withstand the higher rate and retain good time resolution using multiwire proportional
830 chambers with orthogonal segmented cathode planes.

831 The MS also gives nanosecond tracking information for triggering on muon tracks. This
832 is accomplished using Resistive Plate Chambers (RPC) in the barrel region $|\eta| < 1.05$
833 and Thin Gap Chambers (TGC) in the end-cap $1.05 < |\eta| < 2.4$ region. Both chamber
834 systems deliver a triggerable signal with a spread of 15–25 ns, thus providing the ability
835 to tag individual beam-crossings.

836

Part III

837

The HbbISR Analysis

838 **Chapter 6**

839 **Data and Simulation Preparation**

840 In order to compare data to theory ATLAS has developed an analysis chain which runs
841 both real data and simulated samples through the same processing, assuring a final
842 result which is as comparable as possible.

843 **6.1 Data Used**

844 **6.2 Monte Carlo Samples**

845 **Chapter 7**

846 **Physics Object Selection**

847 After the ATHENA Digitization step both data and monte carlo have the same format,
848 representing the three dimentional energy deposits. In order to analyze these deposits
849 they are cleaned, clustered and checked for overlap resulting in physics objects useful
850 for our specific analysis.

851 **7.1 Calorimeter Jets**

852 **7.2 Track Jets**

853 **7.3 Fat Jets**

854 **7.4 B-tagged Jets**

855 **7.5 Muons**

856 **7.6 Overlap Removal**

857 **Chapter 8**

858 **Event Selection**

859 Having created our physics objects we begin to make selections of what types of events
860 we want to consider given the goal of our analysis. In our boosted topology this means
861 considering things like momentum, jet collection efficiencies and background rejection.

862 **8.1 Selected Triggers**

863 **8.2 Pre-selection Studies**

864 **8.3 Signal Selection**

865 **8.4 Optimisation**

866 Chapter 9

867 Background Estimation

868 The dominant background was QCD. I worked on the ttbar control region. The Vqq
869 and single top backgrounds were estimated from monte carlo.

870 9.1 Multi-jet QCD estimation

871 9.2 $t\bar{t}$ control region

872 9.3 Single top estimation

873 9.4 Hadronic vector boson channel

874 **Chapter 10**

875 **Systematic Uncertainties**

876 **10.1 Theoretical Uncertainties**

877 **10.2 Experimental Uncertainties**

878 **Chapter 11**

879 **Statistical Fit**

880 The statistical fit in our analysis was accomplished using a framework developed for
881 Higgs searches.

882 **11.1 Profile Likelihood Function**

883 **11.2 Fit Configuration**

884 **11.3 Statistical Tests**

885 **Chapter 12**

886 **Results**

887 **12.1 Expectations**

888 **12.2 Statistical Analysis Results**

889 **12.3 Measurements and Limits**

890

Part IV

891

Conclusion

892 Chapter 13

893 Conclusion

894 I conclude that this section is the conclusion

Bibliography

- [1] Particle Data Group. “Review of Particle Physics, Chapter 11: Status of Higgs Boson Physics”. In: *Phys. Rev. D* 98 (3 2018), p. 030001. DOI: 10.1103/PhysRevD.98.030001. URL: <https://link.aps.org/doi/10.1103/PhysRevD.98.030001> (cit. on pp. 22, 24, 27, 29).
- [2] L. A. Harland-Lang et al. “Parton distributions in the LHC era: MMHT 2014 PDFs”. In: *The European Physical Journal C* 75.5 (May 2015), p. 204. ISSN: 1434-6052. DOI: 10.1140/epjc/s10052-015-3397-6. URL: <https://doi.org/10.1140/epjc/s10052-015-3397-6> (cit. on p. 26).
- [3] Georges Aad et al. “Measurements of the Higgs boson production and decay rates and constraints on its couplings from a combined ATLAS and CMS analysis of the LHC pp collision data at $\sqrt{s} = 7$ and 8 TeV”. In: *JHEP* 08 (2016), p. 045. DOI: 10.1007/JHEP08(2016)045. arXiv: 1606.02266 [hep-ex] (cit. on pp. 29–32).
- [4] Lyndon Evans and Philip Bryant. “LHC Machine”. In: *JINST* 3 (2008), S08001. DOI: 10.1088/1748-0221/3/08/S08001 (cit. on p. 35).

- [5] Chris Llewellyn Smith. “Genesis of the Large Hadron Collider”. In: *Phil. Trans. Roy. Soc. Lond.* A373.2032 (2014), p. 20140037. DOI: 10.1098/rsta.2014.0037 (cit. on p. 35).
- [6] ATLAS Collaboration. “The ATLAS Experiment at the CERN Large Hadron Collider”. In: *JINST* 3 (2008), S08003. DOI: 10.1088/1748-0221/3/08/S08003 (cit. on pp. 46, 48, 54–62).
- [7] Giordon Holtsberg Stark. “The search for supersymmetry in hadronic final states using boosted object reconstruction”. Presented 26 Apr 2018. May 2018. URL: <https://cds.cern.ch/record/2317296> (cit. on pp. 50, 51).
- [8] Karolos Potamianos. *The upgraded Pixel detector and the commissioning of the Inner Detector tracking of the ATLAS experiment for Run-2 at the Large Hadron Collider*. Tech. rep. ATL-PHYS-PROC-2016-104. 15 pages, EPS-HEP 2015 Proceedings. Geneva: CERN, Aug. 2016. URL: <https://cds.cern.ch/record/2209070> (cit. on p. 52).
- [9] *ATLAS inner detector: Technical Design Report, 1*. Technical Design Report ATLAS. Geneva: CERN, 1997. URL: <http://cds.cern.ch/record/331063> (cit. on p. 52).
- [10] S Haywood et al. *ATLAS inner detector: Technical Design Report, 2*. Technical Design Report ATLAS. Geneva: CERN, 1997. URL: <https://cds.cern.ch/record/331064> (cit. on p. 52).

- 930 [11] B. Abbott et al. “Production and integration of the ATLAS Insertable B-Layer”.
931 In: *JINST* 13 (2018), T05008. DOI: 10.1088/1748-0221/13/05/T05008. arXiv:
932 1803.00844 [physics.ins-det] (cit. on p. 53).
- 933 [12] Christian Wolfgang Fabjan and F Gianotti. “Calorimetry for Particle Physics”.
934 In: *Rev. Mod. Phys.* 75.CERN-EP-2003-075 (Oct. 2003), 1243–1286. 96 p. DOI:
935 10.1103/RevModPhys.75.1243. URL: <https://cds.cern.ch/record/692252>
936 (cit. on p. 57).

937 **Appendix A**

938 **Hadronic Vqq Sherpa Studies**

939 Ancillary material should be put in appendices, which appear after the bibliography.